ISA Transactions 136 (2023) 345–360

Contents lists available at ScienceDirect

ISA Transactions

journal homepage: www.elsevier.com/locate/isatrans

Research article

3D hybrid formation control of an underwater robot swarm: Switching topologies, unmeasurable velocities, and system constraints

Yuwei Zhang [a,b,c], Shaoping Wang [a,c,*], Mary Katherine Heinrich [b], Xingjian Wang [a], Marco Dorigo [b]

[a] School of Automation Science and Electrical Engineering, Beihang University, 100191 Beijing, China
[b] Institut de Recherches Interdisciplinaires et de Développements en Intelligence Artificielle (IRIDIA), Université Libre de Bruxelles (ULB), Brussels, Belgium
[c] State Key Laboratory of Software Development Environment, Beihang University, 100191 Beijing, China

ARTICLE INFO

Article history:
Received 12 August 2021
Received in revised form 17 November 2022
Accepted 17 November 2022
Available online 26 November 2022

Keywords:
Formation control
Autonomous underwater vehicles
Distributed observer
Switching topologies
System constraints

ABSTRACT

This paper addresses formation control of underactuated autonomous underwater vehicles in three-dimensional space, using a hybrid protocol that combines aspects of centralized and decentralized control with constraints that are particular to underwater vehicles, including switching topologies, unmeasurable velocities, and system constraints. Using a distributed leader–follower model, the hybrid formation protocol does not require velocity sensing, access to global information, or static and connected topologies. To handle switching jointly connected networks—that is, to tolerate temporary disconnections—a distributed observer is designed for followers to cooperatively estimate leader states using local measurements and local interactions. On this basis, a compound formation control strategy is proposed to achieve geometric convergence. Firstly, cascaded extended state observers are developed to recover the unmeasurable velocities and unknown dynamic uncertainties induced by internal model uncertainty and external disturbances. Secondly, an improved three-dimensional line-of-sight guidance law at the kinematic level is used to address the underactuated configuration and the nonzero attack and sideslip angles. Thirdly, to overcome potential instability as a result of system constraints, including velocity constraints and input saturations, two adaptive compensators in the dynamic controller are used to address the negative effects of truncation. Using the proposed approach, the estimation errors and formation tracking errors are proved to be uniformly and ultimately bounded. Additionally, the numerical simulation results verify the performance of the approach and demonstrate improvement over both distributed and centralized state-of-the-art approaches.

1. Introduction

In distributed control of robot swarms, both opinion dynamics and physical coordination have been widely studied. Consensus achievement in swarm robotics has, for instance, been studied in flocking problems and in opinion formation in collective decision-making (e.g., [1]). Formation control, by contrast, is more intensively studied in control theory [2], as noted in [3]. Swarm robotics has advanced significantly in recent years, especially concerning swarms of small, simple ground or aerial robots managed primarily by kinematic control (e.g., [4,5]). However, swarms of other robot types such as autonomous underwater vehicles (AUVs) require the consideration of new practical challenges, as do tasks such as formation control that have not frequently been studied in swarm robotics. These challenges are difficult to address with purely decentralized control, even from a swarm robotics perspective—instead, they are well-suited to hybrid control approaches that combine aspects of centralized and decentralized control, and which are recently becoming more common in swarm robotics research [e.g., with hierarchy6–8]. Likewise, formation protocols for AUVs are becoming more widespread, but some important practical challenges of underwater swarms have not yet been integrated theoretically.

1.1. Motivations

Although formation control of AUVs has received much recent attention (as reported in [9]), the state of the art still has several important gaps that prevent theoretical studies from being transferred to applications. The paper addresses the following three challenges that are of practical importance for formation control of AUV swarms:

- **Network reliability:** To achieve the desired behavior cooperatively, AUVs are required to exchange information using wireless communication. In underwater environments,

* Corresponding author.
E-mail address: shaopingwang@vip.sina.com (S. Wang).

https://doi.org/10.1016/j.isatra.2022.11.014
0019-0578/

the most commonly used technique is acoustic communication, due to its low attenuation. In addition to intrinsic constraints such as limited bandwidth and range, acoustic communication is not perfectly reliable. As with many communication techniques, the occurrence of occasional link failures is inevitable. Additionally, the reliability of acoustic communication can be greatly affected by environmental conditions such as temperature and salinity [10]. Overall, network unreliability in underwater conditions means that it is difficult or impossible to maintain a connected and static communication topology in an AUV swarm in practice. It is therefore of great importance to study not only graphs with switching topologies, but also graphs that can have disconnections.

- **Position and velocity measurement:** Formation protocols in the literature normally require both global position and velocity measurements, essentially transforming the problem of formation control of the swarm into simple single-vehicle trajectory tracking for each AUV separately. However, in underwater robot swarms there are problems with assuming that both the global position and velocity measurements will be available. Regarding the former, real global position information needs to be based on pre-deployed and localized infrastructures, and in practice it is difficult for AUVs to consistently make use of widely available infrastructure such as GPS, due to signal attenuation problems [11]. Realistically, underwater robot swarms should be assumed to operate (at least some of the time) in GPS-denied environments, in which AUVs need to directly measure their relative positions to their neighbors (e.g., using simultaneous localization and mapping, monocular vision feature matching, or baseline acoustic positioning [12]). Regarding the latter, if real AUVs can be equipped with velocity sensors at all (which might be prohibitively too costly and/or heavy), accurate velocity measurements are still an unresolved challenge due to sensor noise and oceanic disturbances [13]. This motivates the development of a velocity-free formation protocol using relative position measurements, which is important for reliability in a challenging environment such as deep water.
- **Velocity constraints:** In order to meet safety and formation tracking performance requirements, a formation protocol must keep the velocities and control inputs of AUVs within certain compact sets. Any violation of these system constraints could result in degraded or even unstable behavior [14]. In the literature, control input constraints have been covered extensively (e.g., [15]), but velocity constraints in AUVs have rarely been discussed. The exceptions are some optimization-based methods (e.g., reference governor [14,16] or model predictive control [17]) to meet velocity constraints. However, because these approaches solve the optimization problem online, their efficacy is dependent on whether the formulated optimization problem can be solved reliably and quickly enough in real time. In this sense, existing protocols do not necessarily guarantee velocity constraint satisfaction. Therefore, AUV formation protocol with guaranteed system constraint satisfaction, which is crucial for the practical handling of real AUVs, can be considered an unsolved challenge.

To address the challenge of network reliability, this paper studies formation control for AUV swarms that can have switching jointly connected topologies. To address the challenges of position and velocity measurement and velocity constraints, it studies formation control that does not require velocity sensing but still guarantees velocity constraint satisfaction. In other words, instead of being exclusive to velocity sensing, this paper studies formation control that can be combined with any sensing technique that can be used to calculate relative position.

1.2. Related work

Approaches to the formation control problem are numerous, but few of them are suitable for AUVs. Table 1 summarizes the state of the art in terms of the main contributions of this paper—i.e., summarizes existing approaches in terms of the topology types that were considered, the measurements required for the approach, the constraints for which satisfaction can be guaranteed, and the dimensions handled. For marine vehicles, leader–follower strategies have been widely studied because of their simplicity and scalability, ranging from two-dimensional (2D) plane (e.g. [18,19,22,23,26]) to three-dimensional (3D) space (e.g. [17,20,21,24,25,27]).

Note that the above approaches are applicable only if the communication topology is static. Such an assumption does not hold practically in an underwater environment. In [28], sufficient conditions were derived to achieve the target formation under both fixed and switching topologies, and in [29,30], Yan et al. addressed discrete-time formation control for AUVs subject to weak communication constraints, including switching topologies and packet losses. Even so, all possible topologies in [28–30] are supposed to be connected. Therefore, it is more relevant to investigate formation control under switching jointly connected topologies–topologies that might be disconnected.

One key limitation of existing approaches for AUVs is the reliance on mandatory velocity measurements for each vehicle (as shown in Table 1), despite velocities being unmeasurable. Velocity sensors, e.g., Doppler Velocity Log, are active sensing devices with high energy consumption, and are difficult to integrate in small and low-cost vehicles with limited payload capacity. In addition, velocity information cannot be calculated via direct derivative/filtering of global position for the following reasons: i) accurate global position measurements should be performed at a relatively high update rate, which is not possible when AUVs are in deep underwater conditions; and ii) even if GPS signals are available near the surface, the numerical differentiation of noisy position measurements leads to chattering of the actuators, and the use of low-pass filters on the numerically reconstructed velocities could deteriorate the tracking performance. An admissible way to recover the unmeasurable states is by using observers [31]. In [26], velocity sensors were replaced by introducing an auxiliary finite-time velocity observer, however only AUVs in a horizontal plane were considered. The velocity observer design in 3D space is more complicated due to highly coupled kinematics and strong nonlinear dynamics. An initial study on this topic is presented in [27], wherein a state-transformation-based velocity observer was designed based on neural networks. However, global position should still be consistently measurable in order to employ the velocity observer proposed by [27]. To the best of the authors' knowledge, velocity-free formation control of AUV swarms is still an open challenge in 3D space, especially when only relative position measurement is available. This is an important gap to address, as velocities are often unmeasurable and there are many alternatives (i.e., velocity-free GPS-denied positioning techniques) available [12].

Another shortcoming of the existing methods is that they cannot preserve optimal control performance under system constraints comprehensively. As seen in Table 1, input saturations have been investigated for formation control of AUVs, for instance in [22–25], but none of these studies have included velocity constraints. By contrast, in [17], a receding horizon algorithm was designed to achieve a prescribed geometric pattern with satisfaction of velocity saturations, but input constraints were not studied. In [14,16], reference governors (RGs) were used to optimize command signals within system constraints, to handle both velocity and input saturations. Note that, because both of

Table 1
Differences among existing formation control approaches for AUV swarms.

		Required measurements		Guaranteed Constraints		Dimension		Reference
		Position	Velocity	Input	Velocity	2D	3D	
Topology	Fixed	✓	✓			✓		[18,19]
		✓	✓				✓	[20,21]
		✓	✓	✓		✓		[22,23]
		✓	✓	✓			✓	[24,25]
		✓	✓		✓		✓	[17]
		✓		✓		✓		[26]
		✓					✓	[27]
	Switching and connected topologies	✓	✓			✓		[28]
		✓	✓				✓	[29,30]

these are optimization-based methods, a feasible solution must be newly found in each control cycle. Therefore, in cases where it is non-trivial to solve the formulated optimization problem in real time, constraint satisfaction is not in this sense guaranteed.

1.3. Contributions

Motivated by the current gaps in the state of the art, this research proposes a hybrid formation protocol for underactuated AUVs in 3D space. The main contributions are summarized as follows:

- The proposed formation protocol is verified to be effective under switching jointly connected topologies (i.e., topologies that might be disconnected at any time), thus relaxing the assumptions in the existing literature of static topologies [17–27] or switching but connected topologies [28–30]. This is realized by the proposed distributed observer (DO), through which each follower estimates the leader's information.
- The proposed formation protocol removes the limitation of reliance on velocity sensing, as compared to [17–25]. The unmeasurable velocities, as well as the dynamic uncertainties, are recovered by the proposed cascaded extended state observer (CESO), which is constructed by state and coordinate transformations to satisfy a standard integral-chain form.
- In addition to input saturation as covered in [22–26], the proposed approach simultaneously guarantees velocity constraint satisfaction, without relying on optimization-based methods [14,16,17] that are not guaranteed to be effective due to the need of finding a solution in every control cycle. To this end, two adaptive wind-up compensators are introduced to alleviate the negative effect of nonlinear saturations on system stability.

1.4. Paper organization

The paper is organized as follows. First, Section 2 introduces the preliminaries, including graph theory and underactuated AUV modeling, and formulates the formation control problem. Then the proposed hybrid formation protocol is introduced in two parts: the design and analysis of the DO (Section 3) and compound velocity-free formation control (Section 4). Finally, the closed-loop system stability under the proposed method is analyzed (Section 5), the comparative simulation results are presented (Section 6), and the paper is concluded.

Notation. $\mathbb{R}^{n\times m}$ denotes the set of $n \times m$ real matrices. $|\cdot|$ and $\|\cdot\|$ denote the L_1-norm and L_2-norm. $\lambda_{\min}(\cdot)$ is the smallest eigenvalue of a square matrix. $\boldsymbol{R}_A^B(\alpha,\beta) = \boldsymbol{R}_z(\alpha)\boldsymbol{R}_y(\beta)$ is the rotation matrix from frame $\{A\}$ to frame $\{B\}$ with $\boldsymbol{R}_z(\alpha) = [\cos\alpha, -\sin\alpha, 0; \sin\alpha, \cos\alpha, 0; 0, 0, 1]$ and $\boldsymbol{R}_y(\beta) = [\cos\beta, 0, \sin\beta; 0, 1, 0; -\sin\beta, 0, \cos\beta]$. $\mathrm{sgn}(\cdot)$ is the sign function, and $\mathrm{sig}^{\alpha}(\boldsymbol{x}) = \mathrm{sgn}(\boldsymbol{x})|\boldsymbol{x}|^{\alpha}$, where $\alpha \geq 0$.

2. Preliminaries and problem formulation

2.1. Graph theory

In leader–follower formation control, the interactions among N followers can be modeled by an undirected graph $\mathcal{G} = (\mathcal{V}, \mathcal{E})$, in which $\mathcal{V} = \{1, \ldots, N\}$ is a set of nodes, $\mathcal{E} = \{(i,j) : i,j \in V, i \neq j\}$ is a set of edges. The adjacency matrix of graph $\mathcal{G}$ is denoted by $\boldsymbol{A} = [a_{ij}] \in \mathbb{R}^{N\times N}$ with nonnegative weights. If $(i,j) \in \mathcal{E}$, $a_{ij} = 1$, otherwise $a_{ij} = 0$. Note that $a_{ii} = 0$, $\forall i \in \mathcal{V}$. The neighbor set of follower i is $\mathcal{N}_i = \{j \in \mathcal{V}, (i,j) \in \mathcal{E}\}$. The Laplacian matrix $\boldsymbol{L} = [l_{ij}]_{N\times N}$ is defined as follows: $l_{ij} = -a_{ij}$ if $i \neq j$, and $l_{ij} = \sum_{j=1}^{N} a_{ij}$ if $i = j$. Communication links between the leader and followers can be characterized by adjacency matrix $\boldsymbol{B} = \mathrm{diag}\{b_1, \ldots, b_N\}$, where $b_i = 1$ if follower i connects to the leader. Let the leader be represented by node 0, and derive the augmented graph $\bar{\mathcal{G}} = (\bar{\mathcal{V}}, \bar{\mathcal{E}})$, where $\bar{\mathcal{V}} = \mathcal{V} \cup \{0\}$ and $\bar{\mathcal{E}}$ includes $\mathcal{E}$ and also includes edges between leader and followers. Denote matrix $\boldsymbol{H} \in \mathbb{R}^{N\times N}$ as $\boldsymbol{H} = \boldsymbol{L} + \boldsymbol{B}$.

The graphs of the AUVs are assumed to be dynamically switching. Denote all possible graphs of multiple AUVs as $S = \{\bar{\mathcal{G}}_q : q \in \mathcal{Q}\}$, where $\mathcal{Q}$ is an index set of S. Consider an infinite sequence of non-overlapping bounded time intervals $[t_k, t_{k+1})$ with $k = 0, 1, \ldots$ and $t_0 = 0$. In $[t_k, t_{k+1})$, there exists a finite time sequence $t_k^0, t_k^1, \ldots, t_k^{l_k-1}$, where $t_k^0 = t_k$ and $t_k^{l_k} = t_{k+1}$ for some integer $l_k > 0$. The graph switches at time t_k^j, $j = 0, 1, \ldots, l_k - 1$ and is time-invariant in the subinterval $[t_k^j, t_k^{j+1})$. Assume that there exists a constant number $\tau > 0$ called dwell time, such that $t_k^{j+1} - t_k^j > \tau$ for all time intervals. Denote $\sigma(t) : [0, +\infty) \to \mathcal{Q}$ as the switching signal. The undirected graph $\bar{\mathcal{G}}$ and matrix $\boldsymbol{H}$ at $\sigma(t)$ are therefore noted respectively as $\bar{\mathcal{G}}_{\sigma(t)}$ and matrix $\boldsymbol{H}_{\sigma(t)}$. Note that $\bar{\mathcal{G}}_{\sigma(t)}$ is allowed to be disconnected. A collection of graphs across the time interval $[t, t+T]$ with $T > 0$ is jointly connected if $\{\bar{\mathcal{G}}_{\sigma(s)} | s \in [t, t+T]\}$ is connected. For each $q \in \mathcal{Q}$, $\boldsymbol{H}_q$ has N eigenvalues denoted as $\lambda_q^1, \lambda_q^2, \ldots, \lambda_q^N$ based on the labeling rule given in [32]. Define $\mathcal{C}(q) = \{k | \lambda_q^k \neq 0, k = 1, 2, \ldots, N\}$ and note the following lemma:

Lemma 1 ([32]). *The graphs are jointly connected across $[t_k, t_{k+1})$, if $\bigcup_{t\in[t_k,t_{k+1})} \mathcal{C}(\sigma(t)) = \{1, \ldots, N\}$.*

2.2. Model of underactuated AUV

Allow the subscript i to represent the variables associated with the ith follower, for the remainder of this paper. To describe the AUV's motion, three reference frames are employed (see Fig. 1(a)): earth-fixed frame $\{I\}$, body-fixed frame $\{B_i\}$ and resultant velocity frame $\{W_i\}$. For $i = 1, \ldots, N$, assume the origins of $\{B_i\}$ and $\{W_i\}$ coincides with the center of gravity of the AUV M_i. The 5-DOF kinematic and dynamic model described in [33] is used for the ith AUV:

$$\begin{cases} \dot{\boldsymbol{\zeta}}_i = \boldsymbol{T}(\theta_i, \psi_i)\boldsymbol{v}_i \\ \boldsymbol{M}_i\dot{\boldsymbol{v}}_i + \boldsymbol{C}_i(\boldsymbol{v}_i)\boldsymbol{v}_i + \boldsymbol{D}_i(\boldsymbol{v}_i)\boldsymbol{v}_i + \boldsymbol{g}_i = \boldsymbol{\tau}_i + \boldsymbol{\tau}_{di} \end{cases},$$

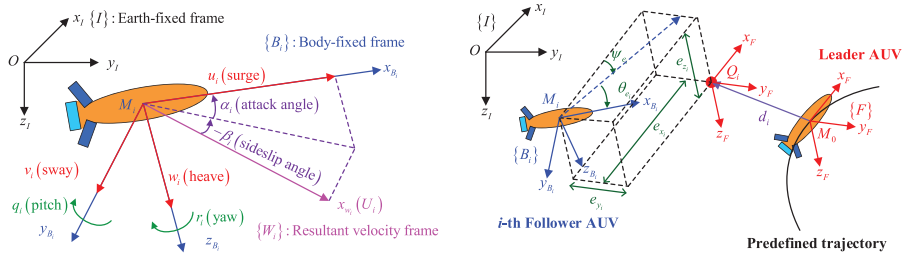

Fig. 1. (a). Frame definitions of an underactuated AUV. (b) Leader–follower formation control problem.

$$\boldsymbol{T} = \begin{pmatrix} \cos\theta_i\cos\psi_i & -\sin\psi_i & \sin\theta_i\cos\psi_i & 0 & 0 \\ \cos\theta_i\sin\psi_i & \cos\psi_i & \sin\theta_i\sin\psi_i & 0 & 0 \\ -\sin\theta_i & 0 & \cos\theta_i & 0 & 0 \\ 0 & 0 & 0 & 1 & 0 \\ 0 & 0 & 0 & 0 & 1/\cos\theta_i \end{pmatrix} \quad (1)$$

where $\boldsymbol{\zeta}_i = [x_i, y_i, z_i, \theta_i, \psi_i]^T$, with x_i, y_i, z_i being the coordinates of M_i in frame $\{I\}$, and θ_i and ψ_i being the pitch and yaw angles. $\boldsymbol{v}_i = [u_i, v_i, w_i, q_i, r_i]^T$ denotes the velocity vector on surge, sway, heave, pitch, and yaw directions expressed in frame $\{B_i\}$. $\boldsymbol{M}_i \in \mathbb{R}^{5\times5}$ is the inertia matrix with added mass, $\boldsymbol{C}_i \in \mathbb{R}^{5\times5}$ is the centripetal and Coriolis matrix, $\boldsymbol{D}_i \in \mathbb{R}^{5\times5}$ is the damping matrix, $\boldsymbol{g}_i \in \mathbb{R}^5$ denotes the restoring forces and moments due to gravity and buoyancy, $\boldsymbol{\tau}_i \in \mathbb{R}^5$ is the control input vector, $\boldsymbol{\tau}_{di} = \left[\tau_{dui}, \tau_{dvi}, \tau_{dwi}, \tau_{dqi}, \tau_{dri}\right]^T$ denotes the dynamic uncertainties, including unmodeled hydrodynamics and external disturbances.

Concerning the controllability and observability of AUVs, the following assumption is made.

Assumption 1 ([33]). (a) The torpedo-shaped AUVs have port/starboard and bottom/top symmetries so that $\boldsymbol{M}_i$ and $\boldsymbol{D}_i$ are diagonal and $\boldsymbol{C}_i$ is skew-symmetric. (b) The center of gravity and the center of buoyancy are located vertically on the z_{Bi} axis. (c) $|\theta_i| \neq \pi/2$.

Under Assumption 1, the dynamic model can be reformulated in the following differential form

$$\begin{cases} \dot{u}_i = (m_{vi}v_ir_i - m_{wi}w_iq_i - d_{ui}u_i)/m_{ui} + sat\,(\tau_{ui})/m_{ui} + \tau_{dui}/m_{ui} \\ \quad = sat\,(\tau_{ui})/m_{ui} + D_{ui} \\ \dot{v}_i = (-m_{ui}u_ir_i - d_{vi}v_i)/m_{vi} + \tau_{dvi}/m_{vi} = D_{vi} \\ \dot{w}_i = (m_{ui}u_iq_i - d_{wi}w_i)/m_{wi} + \tau_{dwi}/m_{wi} = D_{wi} \\ \dot{q}_i = \left((m_{wi} - m_{ui})\,u_iw_i - d_{qi}q_i - G_i\nabla_i\sin\theta_i\right)/m_{qi} + sat\left(\tau_{qi}\right)/m_{qi} \\ \quad + \tau_{dqi}/m_{qi} = sat\left(\tau_{qi}\right)/m_{qi} + D_{qi} \\ \dot{r}_i = ((m_{ui} - m_{vi})\,u_iv_i - d_{ri}r_i)/m_{ri} + sat\,(\tau_{ri})/m_{ri} + \tau_{dri}/m_{ri} \\ \quad = sat\,(\tau_{ri})/m_{ri} + D_{ri} \end{cases}, \quad (2)$$

where $m_{(\cdot)i}$ and $d_{(\cdot)i}$ are inertia and hydrodynamic damping coefficients, respectively; G_i is submerged weight; ∇_i is the distance between the center of gravity and the center of buoyancy; $D_{(\cdot)i}$ denotes the lumped uncertainties including unknown hydrodynamics and environmental disturbances; and $sat\,(\cdot)$ is the input saturation function to be defined later.

Given the inherent operation ranges of the propeller and control surfaces of AUVs, $\tau_{(\cdot)i}$ are naturally bounded [24]. $\boldsymbol{v}_i$ is expected to remain within certain prescribed compact sets for performance and safety considerations. Therefore, the saturation nonlinearity is given by

$$sat\,(x_i) = \begin{cases} x_i^{\max}, x_i > x_i^{\max} \\ x_i, x_i^{\min} \le x_i \le x_i^{\max} \\ x_i^{\min}, x_i < x_i^{\min} \end{cases}, \quad x = u, q, r, \tau_u, \tau_q, \tau_r \quad , \quad (3)$$

where $x_i^{\max}$ and $x_i^{\min}$ are the upper and lower bounds, respectively. Note that there are no control inputs in the sway and heave directions. It is commonly assumed that v_i and w_i are passively bounded, and therefore will not be considered in the controller design [2,18].

From Eq. (2), it can be observed that AUVs suffer from variations in the sway and heave directions. Therefore, the resultant velocity direction of an AUV is not parallel to the surge direction, which causes nonzero and time-varying attack angle $\alpha_i = \arctan\left(w_i/u_i\right)$ and sideslip angle $\beta_i = \arctan\left(v_i/\sqrt{u_i^2 + w_i^2}\right)$. Define $\boldsymbol{v}_{W_i} = [U_i, 0, 0]^T$, with $U_i = \sqrt{u_i^2 + v_i^2 + w_i^2}$, $\boldsymbol{v}_{B_i} = [u_i, v_i, w_i]^T$, which represents the resultant velocity of an AUV in frames $\{W_i\}$ and $\{B_i\}$. Then, the following transformation exists: $\boldsymbol{v}_{W_i} = \boldsymbol{R}_{B_i}^{W_i}(-\beta_i, \alpha_i)\,\boldsymbol{v}_{B_i}$.

2.3. Leader–follower formation tracking error dynamics

The leader–follower formation control problem is illustrated in Fig. 1(b), wherein a group of AUVs is required to achieve a desired formation with respect to the leader M_0. Note that the motion control of the leader is not considered, and the leader is assumed to move on a predefined trajectory. Denote the position of M_0 in $\{I\}$ frame as $\boldsymbol{p}_0(t) = [x_0(t), y_0(t), z_0(t)]^T$. Associated with M_0, Serret–Frenet frame $\{F\}$ is built. Let $\boldsymbol{R}_I^F = \left(\boldsymbol{R}_F^I(\chi_0, \upsilon_0)\right)^T$ denote the rotation matrix from frame $\{F\}$ to frame $\{I\}$, where $\chi_0 = \text{atan2}\left(\dot{y}_0(t), \dot{x}_0(t)\right)$ and $\upsilon_0 = \arctan\left(-\dot{z}_0(t)/\sqrt{\dot{x}_0^2(t) + \dot{y}_0^2(t)}\right)$.

Define $\boldsymbol{p}_i = [x_i, y_i, z_i]^T$ as the inertial position of M_i and $\boldsymbol{h}_i = \left[d_{xi}, d_{yi}, d_{zi}\right]^T$ as the desired relative position between M_i and M_0. Then, the formation tracking error built in frame $\{F\}$ is given by $\boldsymbol{e}_{pi} = \left[e_{xi}, e_{yi}, e_{zi}\right]^T = \boldsymbol{R}_I^F\left(\boldsymbol{p}_i - \boldsymbol{p}_0 - \boldsymbol{h}_i\right)$.

Remark 1. The formation tracking error in [34,35] is defined as $\boldsymbol{e}_{pi}(t) = \sum_{j\in\mathcal{N}_i}\left(\boldsymbol{p}_i(t) - \boldsymbol{h}_i\right) - \left(\boldsymbol{p}_j(t) - \boldsymbol{h}_j\right)$. Note that this requires that the neighbor set $\mathcal{N}_i$ is not empty (i.e., that no vehicle is temporarily disconnected from all other vehicles at any time). By contrast, our formation tracking error is directly defined between leader and followers and a distributed observer will be designed later for followers to cooperatively estimate leader information over jointly connected topologies (as shown in Assumption 2), which tolerates temporary isolations of AUVs. Therefore, the assumption of consistently connected graphs in [34,35] is relaxed.

Differentiating $\boldsymbol{e}_{pi}$ with respect to time yields

$$\begin{aligned}\dot{\boldsymbol{e}}_{pi} &= \boldsymbol{S}_I^F \boldsymbol{e}_{pi} + \boldsymbol{R}_I^F \dot{\boldsymbol{p}}_i - \boldsymbol{v}_0 \\ &= \boldsymbol{S}_I^F \boldsymbol{e}_{pi} + \boldsymbol{R}_I^F \boldsymbol{R}_{B_i}^I \left(\psi_i, \theta_i\right) \boldsymbol{v}_{B_i} - \boldsymbol{v}_0 \\ &= \boldsymbol{S}_I^F \boldsymbol{e}_{pi} + \boldsymbol{R}_{B_i}^F \left(\psi_{ei}, \theta_{ei}\right) \boldsymbol{v}_{W_i} - \boldsymbol{v}_0 + \boldsymbol{f}_{pi}\end{aligned} \tag{4}$$

where $\boldsymbol{v}_0 = [U_0, 0, 0]^T$, with $U_0 = \sqrt{\dot{x}_0^2 + \dot{y}_0^2 + \dot{z}_0^2}$, $\boldsymbol{S}_I^F = \begin{pmatrix} 0 & \dot{\chi}_0 \cos \upsilon_0 & -\dot{\upsilon}_0 \\ -\dot{\chi}_0 \cos \upsilon_0 & 0 & -\dot{\chi}_0 \sin \upsilon_0 \\ \dot{\upsilon}_0 & \dot{\chi}_0 \sin \upsilon_0 & 0 \end{pmatrix}$, ψ_{ei} and θ_{ei} are rotation angles, and $\boldsymbol{f}_{pi} = \left[f_{xi}, f_{yi}, f_{zi}\right]^T = \boldsymbol{R}_I^F \boldsymbol{R}_{B_i}^I \left(\boldsymbol{v}_{B_i} - \boldsymbol{v}_{W_i}\right)$. Eq. (4) can then be expanded as

$$\begin{cases} \dot{e}_{xi} = e_{yi} \dot{\chi}_0 \cos \upsilon_0 - e_{zi} \dot{\upsilon}_0 + U_i \cos \psi_{ei} \cos \theta_{ei} - U_0 + f_{xi} \\ \dot{e}_{yi} = -e_{xi} \dot{\chi}_0 \cos \upsilon_0 - e_{zi} \dot{\chi}_0 \sin \upsilon_0 + U_i \sin \psi_{ei} \cos \theta_{ei} + f_{yi} \\ \dot{e}_{zi} = e_{xi} \dot{\upsilon}_0 + e_{yi} \dot{\chi}_0 \sin \upsilon_0 - U_i \sin \theta_{ei} + f_{zi} \end{cases} . \tag{5}$$

Remark 2. The nonlinearity $\boldsymbol{f}_{pi}$ is induced by the nonzero attack angle α_i and sideslip angle β_i, because $\boldsymbol{f}_{pi}$ will be equal to zero if $\alpha_i = \beta_i = 0$. From Eq. (5), the effect of attack angle α_i and sideslip angle β_i on the formation tracking performance can clearly be identified. It is therefore important to fully consider this nonlinearity in the controller design.

Remark 3. Conventional tracking error dynamics (e.g., as seen in [36,37]), introduce α_i and β_i in the rotation angles ψ_{ei} and θ_{ei}, defined as $\psi_{ei} = \chi_i - \chi_0$ and $\theta_{ei} = \upsilon_i - \upsilon_0$, where $\chi_i = \psi_i + \beta_i$ and $\upsilon_i = \theta_i + \alpha_i$ are rotation angles from frame $\{W_i\}$ to frame $\{I\}$. Note that although this definition is rigorous in a 2D plane, it cannot always be used in 3D space. Therefore, this paper instead puts forward kinematic nonlinearity $\boldsymbol{f}_{pi}$, based on equivalent coordinate transformation, by which the effects of α_i and β_i are considered in position error dynamics rather than angle error dynamics.

2.4. Problem formulation

The formation control objective in this paper is that, when following a leader moving on a smooth trajectory, a group of underactuated AUVs is able to form a desired 3D geometric pattern, regardless of unmeasurable velocities, system constraints, and switching topologies. This general objective can be partitioned into the following two sub-objectives.

The first is a *distributed estimation objective*. Under switching topologies, the information of the leader, e.g., relative position $\boldsymbol{p}_{ei} = \boldsymbol{p}_i - \boldsymbol{p}_0$, might not be known by all followers, therefore the formation tracking error $\boldsymbol{e}_{pi}$ is not be available for the control design. To address this issue, each follower should estimate the information of the leader in a distributed manner, such that $\lim_{t\to\infty} \left\| \hat{\boldsymbol{\eta}}_{i0}(t) - \boldsymbol{\eta}_{i0}(t) \right\| = 0$, where $\boldsymbol{\eta}_{i0}$ is the later-defined information of the leader, and $\hat{\boldsymbol{\eta}}_{i0}$ represents the estimation of $\boldsymbol{\eta}_{i0}$ by the ith follower.

The second is a *geometric objective*. Under unmeasured velocities, lumped uncertainties, and system constraints, the AUVs should form a desired formation prescribed by $\boldsymbol{d}_i$, such that $\lim_{t\to\infty} \left\| \boldsymbol{e}_{pi}(t) \right\| < \epsilon_p$, where ϵ_p is a small positive constant.

In consideration of physical constraints, three practical assumptions are made.

Assumption 2 (*[23,31]*)**.** For lumped uncertainties in Eq. (2), there exists a positive constant $\bar{D}$, such that $\left\| D_{(\cdot)i} \right\| \le \bar{D}$ and $\left\| \dot{D}_{(\cdot)i} \right\| \le \bar{D}$.

Remark 4. From a practical point of view, lumped uncertainties $D_{(\cdot)i}$ and $\dot{D}_{(\cdot)i}$ are time-varying and unpredictable, but are limited in the sense of energy. To determine an accurate upper bound $\bar{D}$, extensive computational fluid dynamics analysis or tower tank experiment analysis should be performed under various vehicle operating conditions, therefore it is normally difficult to know $\bar{D}$ beforehand. It is worth noting that the proposed method can be performed without this prior knowledge (refer to Theorem 2).

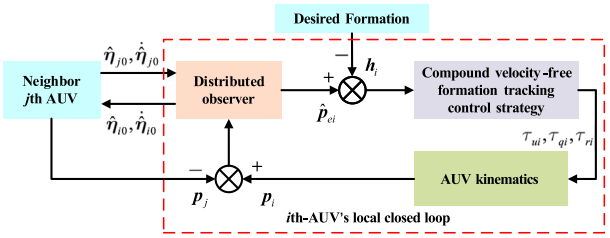

Fig. 2. An overview of the proposed hybrid formation protocol for AUV swarm.

Assumption 3 (*[32]*)**.** The graphs are jointly connected across each interval $[t_k, t_{k+1})$.

Remark 5. Only joint connectivity is required and the graphs are permitted to be disconnected across some subintervals of time. This is distinct from switching topologies in [28–30].

Assumption 4 (*[23]*)**.** There exists a positive constant $\bar{p}$, such that $\left|\dot{\boldsymbol{p}}_0\right| \le \bar{p}$ and $\left|\ddot{\boldsymbol{p}}_0\right| \le \bar{p}$.

Remark 6. Assumption 4 is made because followers need to estimate the information of the leader under switching topologies, and in this case it is indispensable to assume these states to be bounded. Note that $\dot{\boldsymbol{p}}_0$ and $\ddot{\boldsymbol{p}}_0$ are the desired translational speed and acceleration of the formation. To determine the upper bound $\bar{p}$, the formation maneuver requirements as well as the velocity and control input constraints of each AUV need to be taken into account.

To solve the 3D formation control problem outlined here, a hybrid formation protocol is proposed, as shown in Fig. 2. Firstly, to achieve the *distributed estimation objective*, a DO is designed for followers (see Section 3). Secondly, a compound velocity-free formation tracking control strategy is developed to achieve the *geometric objective* (see Section 4).

3. Distributed observer design

Under the leader–follower structure, the information of the leader must be integrated such that followers can track the motion of the leader and maintain the target geometric pattern. This need has inspired the use of AUV interactions to collaboratively estimate leader information using a distributed observer (DO), under static topologies [38] and switching but connected topologies [39]. Note that, in underwater conditions, it should be assumed that the topology will sometimes be disconnected. Efforts to design a DO under switching jointly connected topologies can be found in [40,41]. However, the leader in these two approaches [40,41] was assumed to be a linear system. Note that, in an AUV swarm, the kinematics are nonlinear and the attitudes are not static. This motivates the following contribution: the design of a DO for an AUV swarm under switching jointly connected topologies.

Define the information related to the leader as $\boldsymbol{\eta}_{i0}(t) = [\boldsymbol{p}_{ei}(t), \boldsymbol{s}_0(t)]^T$, where $\boldsymbol{s}_0 = [\chi_0, \upsilon_0, U_0]^T$. Then, assign $\hat{\boldsymbol{\eta}}_{i0}(t) = \left[\hat{\boldsymbol{p}}_{ei}(t), \hat{\boldsymbol{s}}_{i0}(t)\right]^T$ to each follower as the estimation of $\boldsymbol{\eta}_{i0}(t)$,

where $\hat{\boldsymbol{s}}_{i0} = [\hat{\chi}_{i0}, \hat{v}_{i0}, \hat{U}_{i0}]^T$. Finally, define consensus-based neighborhood information estimation error $\boldsymbol{\mu}_{\eta i}$ as $\boldsymbol{\mu}_{\eta i} = \sum_{j=1}^{N} a_{ij}(t)\left(\hat{\boldsymbol{\eta}}_{i0} - \hat{\boldsymbol{\eta}}_{j0}\right) + b_i(t)\hat{\boldsymbol{\eta}}_{i0} + \boldsymbol{\Phi}_{\eta i}$, where $\boldsymbol{\Phi}_{\eta i} = \left[\boldsymbol{\Phi}_{pi}, \boldsymbol{\Phi}_{si}\right]^T$, with $\boldsymbol{\Phi}_{pi} = \sum_{j=1}^{N} a_{ij}\left(\boldsymbol{p}_j - \boldsymbol{p}_i\right) + b_i(\boldsymbol{p}_0 - \boldsymbol{p}_i)$ and $\boldsymbol{\Phi}_{si} = -b_i\boldsymbol{s}_0$. Note that $\boldsymbol{p}_0 - \boldsymbol{p}_i$ and $\boldsymbol{s}_0$ are available for a vehicle if and only if $b_i = 1$. Under Assumption 4 and bounded velocities, there exists a positive constant γ_Φ such that $\left|\dot{\boldsymbol{\Phi}}_{\eta i}\right| \le \gamma_\Phi$.

Remark 7. If velocity constraints are known, $\left|\dot{\boldsymbol{p}}_i\right| \le \left|\boldsymbol{R}_{B_i}^I\right|\left|\boldsymbol{v}_{B_i}\right| \le 3(u_{\max} + v_{\max} + w_{\max}) = \dot{p}_{\max}$ can be derived. Assumption 4 further implies that $\left|\dot{\boldsymbol{\Phi}}_{pi}\right| \le (2N+1)\dot{p}_{\max} + \bar{p}$ and $\left|\dot{\boldsymbol{\Phi}}_{si}\right| \le 2 + \bar{p}$. Therefore, a possible solution for γ_Φ is $\gamma_\Phi = (2N+1)\dot{p}_{\max} + 2(\bar{p}+1)$.

Then, the DO is proposed as

$$\dot{\hat{\boldsymbol{\eta}}}_{i0} = \begin{cases} \dfrac{1}{\alpha_i}\left(-\boldsymbol{K}_\eta\boldsymbol{\mu}_{\eta i} + \sum_{j=1}^{N} a_{ij}\dot{\hat{\boldsymbol{\eta}}}_{j0} - \kappa_1 \mathrm{sgn}\left(\boldsymbol{\mu}_{\eta i}\right) - \kappa_2 \mathrm{sig}^{\varsigma}(\boldsymbol{\mu}_{\eta i})\right), \\ \quad \alpha_i > 0 \\ \boldsymbol{0}, \alpha_i = 0 \end{cases}$$

$$\alpha_i = \sum_{j=1}^{N} a_{ij} + b_i \tag{6}$$

where $\boldsymbol{K}_\eta \in \mathbb{R}^{6\times 6}$ is a diagonal positive definite matrix, κ_1 is a positive constant to be determined, and $\kappa_2 > 0$, ς satisfies $0 < \varsigma = \varsigma_1/\varsigma_2 < 1$ with ς_1 and ς_2 being positive odd integers.

The observer is implemented in a cooperative manner as follows. If the jth follower is the neighbor of the ith AUV, $\hat{\boldsymbol{\eta}}_{j0}$ and $\dot{\hat{\boldsymbol{\eta}}}_{j0}$ are sent to the ith follower via a given underwater communication technique. Meanwhile, the sensor of the ith AUV can measure the relative position $\boldsymbol{p}_i - \boldsymbol{p}_j$. If the leader is the neighbor of the ith follower, $\boldsymbol{s}_0$ and $\boldsymbol{p}_i - \boldsymbol{p}_0$ will be available. Subsequently, the ith follower can calculate $\boldsymbol{\mu}_{\eta i}$ with local information, and update the observer as in Eq. (6). In this sense, the proposed DO is a coordination mechanism in which AUVs directly cooperate using local inter-AUV communication and local measurements.

Theorem 1. *Let $\kappa_1 \ge \gamma_\Phi$. If Assumptions 3 and 4 hold, with the proposed DO in Eq. (6), then the followers can estimate the information of the leader accurately under switching topologies, i.e., the estimation error $\tilde{\boldsymbol{\eta}}_{i0}(t) = \hat{\boldsymbol{\eta}}_{i0}(t) - \boldsymbol{\eta}_{i0}(t)$ converges to zero in finite time. (The proof is given in Appendix A.)*

With the proposed DO Eq. (6), each follower is able to estimate the information of the leader in finite time denoted by T_F. That is, $\boldsymbol{\eta}_{i0}(t) = \hat{\boldsymbol{\eta}}_{i0}(t)$ for $t \ge T_F$. Thus, we can employ $\hat{\boldsymbol{\eta}}_{i0}(t)$ directly in the formation tracking control strategy.

4. Formation tracking control strategy

In this section, a compound velocity-free formation tracking control strategy is designed to achieve the *geometric objective*. First, a cascaded extended state observer (CESO) is proposed to recover unmeasurable velocities and approximate dynamic uncertainties. Second, an improved 3D nonlinear guidance law is developed at the kinematic level. Third, a constrained robust controller is designed at the dynamic level to guarantee the performance of disturbance rejection as well as stability under constraints.

4.1. Cascaded ESO design

The ESO is an essential method in active disturbance rejection control and requires minimal information about a dynamic system, thus it has already been used for AUVs in a horizontal plane [23,31]. However, this conventional ESO cannot directly be used for AUVs in 3D space, for the following two reasons. (i) The kinematics in the yaw direction do not satisfy the integral-connected form. (ii) The conventional ESO requires absolute position measurements, which cannot be guaranteed to be feasible for AUVs in deep water. Therefore, this paper designs a cascaded ESO (CESO) for AUVs in 3D space.

As the first step, for pitch direction, the following ESO is designed to estimate q_i and D_{qi}:

$$\begin{cases} \dot{\hat{\theta}}_i = -k_{q1}\left(\hat{\theta}_i - \theta_i\right) + \hat{q}_i \\ \dot{\hat{q}}_i = -k_{q2}\left(\hat{\theta}_i - \theta_i\right) + \tau_{qi}/m_{qi} + \hat{D}_{qi} \\ \dot{\hat{D}}_{qi} = -k_{q3}\left(\hat{\theta}_i - \theta_i\right) \end{cases}, \tag{7}$$

where $\hat{\theta}$, $\hat{q}_i$, and $\hat{D}_{qi}$ are the respective estimations of θ, q_i, and D_{qi}. k_{q1}, k_{q2}, and k_{q3} are positive constants.

In the second step, in order to construct the integral chain form in yaw direction, a state transformation is performed. Let $\xi_{ri} = \psi_i \cos\theta_i$, then the following ESO to estimate r_i and D_{ri} can be designed:

$$\begin{cases} \dot{\hat{\xi}}_{ri} = -k_{r1}\left(\hat{\xi}_{ri} - \xi_{ri}\right) + \hat{r}_i - \hat{q}_i\psi_i\sin\theta_i \\ \dot{\hat{r}}_i = -k_{r2}\left(\hat{\xi}_{ri} - \xi_{ri}\right) + \tau_{ri}/m_{ri} + \hat{D}_{ri} \\ \dot{\hat{D}}_{ri} = -k_{r3}\left(\hat{\xi}_{ri} - \xi_{ri}\right) \end{cases}, \tag{8}$$

where $\hat{\xi}_{ri}$, $\hat{r}_i$, and $\hat{D}_{ri}$ are the estimations of ξ_{ri}, r_i, and D_{ri}. k_{r1}, k_{r2}, and k_{r3} are positive constants.

In the third step, instead of employing absolute position, the relative position to the leader $\boldsymbol{p}_{ei}$ is utilized and an equivalent coordinate transformation is performed. $\boldsymbol{p}_{ei}$ can be expressed in frame $\{B_i\}$ as $\boldsymbol{\xi}_{pi} = \boldsymbol{R}_I^{B_i}\boldsymbol{p}_{ei}$ and the dynamics can then be derived as follows: $\dot{\boldsymbol{\xi}}_{pi} = \boldsymbol{S}_I^{B_i}(r_i, q_i, \theta_i)\boldsymbol{\xi}_{pi} + \boldsymbol{v}_{B_i} - \boldsymbol{R}_I^{B_i}\dot{\boldsymbol{p}}_0$, $\dot{\boldsymbol{v}}_{B_i} = \boldsymbol{\tau}_{pi} + \boldsymbol{D}_{pi}$, where $\boldsymbol{\tau}_{pi} = [\tau_{ui}/m_{ui}, 0, 0]^T$, $\boldsymbol{D}_{pi} = [D_{ui}, D_{vi}, D_{wi}]^T$, $\boldsymbol{R}_I^{B_i} = \left(\boldsymbol{R}_{B_i}^I(\psi_i, \theta_i)\right)^T$, $\boldsymbol{S}_I^{B_i} = \begin{pmatrix} 0 & r_i & -q_i \\ -r_i & 0 & -r_i\tan\theta_i \\ q_i & r_i\tan\theta_i & 0 \end{pmatrix}$, $\boldsymbol{\zeta}_i = [x_i, y_i, z_i, \theta_i, \psi_i]^T$. Based on the above dynamics, the following ESO is designed:

$$\begin{cases} \dot{\hat{\boldsymbol{\xi}}}_{pi} = -\boldsymbol{K}_{p1}\left(\hat{\boldsymbol{\xi}}_{pi} - \boldsymbol{\xi}_{pi}^e\right) + \boldsymbol{S}_I^{B_i}\left(\hat{r}_i, \hat{q}_i, \theta_i\right)\boldsymbol{\xi}_{pi}^e + \hat{\boldsymbol{v}}_{B_i} - \boldsymbol{R}_I^{B_i}\dot{\boldsymbol{p}}_0^e \\ \dot{\hat{\boldsymbol{v}}}_{B_i} = -\boldsymbol{K}_{p2}\left(\hat{\boldsymbol{\xi}}_{pi} - \boldsymbol{\xi}_{pi}^e\right) + \hat{\boldsymbol{D}}_{pi} + \boldsymbol{\tau}_{pi} \\ \dot{\hat{\boldsymbol{D}}}_{pi} = -\boldsymbol{K}_{p3}\left(\hat{\boldsymbol{\xi}}_{pi} - \boldsymbol{\xi}_{pi}^e\right) \end{cases}, \tag{9}$$

where $\boldsymbol{K}_{p1} \in \mathbb{R}^{3\times 3}$, $\boldsymbol{K}_{p2} \in \mathbb{R}^{3\times 3}$ and $\boldsymbol{K}_{p3} \in \mathbb{R}^{3\times 3}$ are diagonal positive definite matrices; and $\hat{\boldsymbol{\xi}}_{pi}$, $\hat{\boldsymbol{v}}_{B_i} = \left[\hat{u}_i, \hat{v}_i, \hat{w}_i\right]^T$, and $\hat{\boldsymbol{D}}_{pi} = [\hat{D}_{ui}, \hat{D}_{vi}, \hat{D}_{wi}]^T$ are respective estimations of $\boldsymbol{\xi}_{pi}$, $\boldsymbol{v}_{B_i}$, and $\boldsymbol{D}_{pi}$. $\boldsymbol{\xi}_{pi}^e = \boldsymbol{R}_I^{B_i}\hat{\boldsymbol{p}}_{ei}$ and $\dot{\boldsymbol{p}}_0^e = \hat{U}_{i0}\left[\cos\hat{\chi}_{i0}\cos\hat{v}_{i0}, \sin\hat{\chi}_{i0}\cos\hat{v}_{i0}, -\sin\hat{v}_{i0}\right]^T$ are defined based on the estimation results of the DO.

Let the velocity estimation error vector be $\tilde{\boldsymbol{v}}_i = \left[\tilde{u}_i, \tilde{v}_i, \tilde{w}_i, \tilde{q}_i, \tilde{r}_i\right]^T$ and the uncertainty estimation error vector be $\tilde{\boldsymbol{D}}_i = \left[\tilde{D}_{ui}, \tilde{D}_{vi}, \tilde{D}_{wi}, \tilde{D}_{qi}, \tilde{D}_{ri}\right]^T$, where $\tilde{\rho}_i = \hat{\rho}_i - \rho_i$ and $\tilde{D}_{\rho i} = \hat{D}_{\rho i} - D_{\rho i}$, $(\rho = u, v, w, q, r)$. Then the CESO Eqs. (7), (8), (9) has the following property.

Theorem 2. *Considering the CESO Eqs. (7), (8), (9) under Assumptions 1–4, $\tilde{\boldsymbol{v}}_i$ and $\tilde{\boldsymbol{D}}_i$ are ultimately bounded. (The proof is given in Appendix B.)*

4.2. Improved 3D kinematic guidance law

Line-of-sight (LOS) guidance is commonly used in motion control of marine vehicles. However, conventional LOS has limited robustness against external disturbances. To enhance the performance, improved LOS guidance laws were developed, as summarized in [42]. However, most methods in [42] only considered a 2D plane. In the research, the existing methods are extended to 3D space.

Before proceeding with the guidance law, define the estimation-based information needed as $\hat{\boldsymbol{e}}_{pi} = \left[\hat{e}_{xi}, \hat{e}_{yi}, \hat{e}_{zi}\right]^T = \left(\boldsymbol{R}_F^I\left(\hat{\chi}_{i0}, \hat{\upsilon}_{i0}\right)\right)^T\left(\hat{\boldsymbol{p}}_{ei} - \boldsymbol{d}_i\right)$, $\hat{\boldsymbol{f}}_{pi} = \left[\hat{f}_{xi}, \hat{f}_{yi}, \hat{f}_{zi}\right]^T = \left(\boldsymbol{R}_F^I\left(\hat{\chi}_{i0}, \hat{\upsilon}_{i0}\right)\right)^T \boldsymbol{R}_{B_i}^I\left(\hat{\boldsymbol{v}}_{B_i} - \hat{\boldsymbol{v}}_{W_i}\right)$, $\hat{U}_i = \sqrt{\hat{u}_i^2 + \hat{v}_i^2 + \hat{w}_i^2}$ and $\hat{\boldsymbol{v}}_{W_i} = \left[\hat{U}_i, 0, 0\right]^T$, where $\hat{\boldsymbol{e}}_{pi}$, $\hat{U}_i$, $\hat{\boldsymbol{\mu}}_{W_i}$, and $\hat{\boldsymbol{f}}_{pi}$ are the estimations of $\boldsymbol{e}_{pi}$, U_i, $\boldsymbol{\mu}_{W_i}$, and $\boldsymbol{f}_{pi}$. Define the desired rotation angles ψ_{ei}^d and θ_{ei}^d such that

$$\psi_{ei}^d = \tan^{-1}\left(-\left(\hat{e}_{yi} + \delta_{yi}\right)/\Delta_y\right), \quad \theta_{ei}^d = \tan^{-1}\left(\left(\hat{e}_{zi} + \delta_{zi}\right)/\Delta_z\right), \tag{10}$$

where Δ_y and Δ_z can be termed look-ahead distances, satisfying $\Delta_z = \sqrt{\Delta_y^2 + \left(\hat{e}_{yi} + \delta_{yi}\right)^2}$. The auxiliary terms δ_{yi} and δ_{zi} take the form

$$\begin{aligned}
\delta_{yi} &= \left(\hat{e}_{yi}\gamma_{yi}^2 + \gamma_{yi}\sqrt{\Delta_y^2\left(1-\gamma_{yi}^2\right) + \hat{e}_{yi}^2}\right)/\left(1-\gamma_{yi}^2\right),\\
\delta_{zi} &= \left(\hat{e}_{zi}\gamma_{zi}^2 + \gamma_{zi}\sqrt{\Delta_z^2\left(1-\gamma_{zi}^2\right) + \hat{e}_{zi}^2}\right)/1-\gamma_{zi}^2,
\end{aligned} \tag{11}$$

where $\gamma_{yi} = \hat{f}_{yi}/\hat{U}_i$ and $\gamma_{zi} = \hat{f}_{zi}/\hat{U}_i$.

To steer ψ_{ei} and θ_{ei} to the desired angles ψ_{ei}^d and θ_{ei}^d, recall $\boldsymbol{R}_F^I\left(\hat{\chi}_{i0}, \hat{\upsilon}_{i0}\right)\boldsymbol{R}_{B_i}^F\left(\psi_{ei}^d, \theta_{ei}^d\right) = \boldsymbol{R}_{B_i}^I\left(\psi_i^d, \theta_i^d\right)$, thus the desired orientation angles can be derived as $\theta_i^d = \arcsin\left(\sin\hat{\upsilon}_{i0}\cos\theta_{ei}^d\cos\psi_{ei}^d + \cos\hat{\upsilon}_{i0}\sin\theta_{ei}^d\right)$, $\psi_i^d = \operatorname{atan2}\left(\psi_i^{dy}, \psi_i^{dx}\right)$, where $\psi_i^{dy} = \sin\hat{\chi}_{i0}\cos\hat{\upsilon}_{i0}\cos\psi_{ei}^d\cos\theta_{ei}^d + \cos\hat{\chi}_{i0}\sin\psi_{ei}^d\cos\theta_{ei}^d - \sin\hat{\chi}_{i0}\sin\hat{\upsilon}_{i0}\sin\theta_{ei}^d$ and $\psi_i^{dx} = \cos\hat{\chi}_{i0}\cos\hat{\upsilon}_{i0}\cos\psi_{ei}^d\cos\theta_{ei}^d - \sin\hat{\chi}_{i0}\sin\psi_{ei}^d\cos\theta_{ei}^d - \cos\hat{\chi}_{i0}\sin\hat{\upsilon}_{i0}\sin\theta_{ei}^d$.

To steer ψ_i and θ_i to ${\psi_i}^d$ and ${\theta_i}^d$, the kinematic controller is designed as

$$\begin{cases}
u_i^d = \left(-b_x\hat{e}_{xi} + \hat{U}_{i0} - \hat{f}_{xi}\right)\cos\alpha_i\cos\beta_i\Delta_i\\
q_i^d = -b_\theta\left(\theta_i - \theta_i^d\right) + \dot{\theta}_i^d\\
r_i^d = \left(-b_\psi\left(\psi_i - {\psi_i}^d\right) + \dot{\psi}_i^d\right)\cos\theta_i
\end{cases}, \tag{12}$$

where b_x, b_θ and b_ψ are positive constants and $\Delta_i = \sqrt{\Delta_y^2 + \left(\hat{e}_{yi} + \delta_{yi}\right)^2 + \left(\hat{e}_{zi} + \delta_{zi}\right)^2}/\Delta_y$.

Remark 8. From Eq. (12), the derivatives of commands are required to implement the kinematic controller. Therefore, the command filter is employed to approximate the derivatives [15]: $\hat{\dot{\theta}}_i^d = \frac{w_n^2 s}{s^2 + 2\xi w_n s + w_n^2}\theta_i^d$, where $\hat{\dot{\theta}}_i^d$ is the estimation of $\dot{\theta}_i^d$, and $w_n > 0$ and $\xi > 0$ are the natural frequency and damp ratios.

4.3. Constrained robust dynamic controller

In this section, a constrained robust controller is designed at the dynamics level, wherein two anti-windup compensators are introduced to address saturations and potential unstable behavior. Due to the similarity of the dynamics models of τ_{ui}, τ_{qi}, and τ_{ri}, only the design process details for τ_{qi} in the pitch direction will be given in detail.

Firstly, note that q_i^d may violate the velocity constraint. To keep the command signal within the constraint, design the velocity command truncation as $\Delta q_i = sat\left(q_i^d - \phi_{qi}\right) - \left(q_i^d - \phi_{qi}\right)$, where ϕ_{qi} is as an anti-windup compensator to regulate the velocity command signal, to be designed later.

Secondly, the control input is intrinsically subject to saturation phenomena. To keep the control input from reaching saturation, design the control input truncation as $\Delta\tau_{qi} = \tau_{qi} - \tau_{qi}^s = sat\left(\tau_{qi}\right) - \tau_{qi}^s$, where $\phi_{\tau qi}$ is an anti-windup compensator to regulate the control input, to be designed later. Then, the following constrained dynamic controller is proposed:

$$\tau_{qi} = m_{qi}\left(-c_q\left(s_{qi} - \phi_{\tau qi}\right) + \dot{q}_i^d - \hat{D}_{qi} - \dot{\phi}_{qi}\right), \tag{13}$$

where $s_{qi} = q_i - q_i^d + \phi_{qi}$ is the regulated velocity tracking error and c_q is a positive constant, to be determined. $\dot{q}_i^d$ can be calculated by command filter. The adaptive laws for ϕ_{qi} and $\phi_{\tau qi}$ are as follows:

$$\begin{aligned}
\dot{\phi}_{qi} &= \begin{cases} -\left(w_1 + \dfrac{w_2\Delta q_i^2}{2\left|\phi_{qi}\right|^2}\right)\phi_{qi} + w_2\Delta q_i, & \left|\phi_{qi}\right| \geq \mu_q \\ 0, & \left|\phi_{qi}\right| < \mu_q \end{cases},\\
\dot{\phi}_{\tau qi} &= \begin{cases} -\left(l_1 + \dfrac{\left|g_{\tau qi}\right| + \frac{l_2\Delta\tau_{qi}^2}{2}}{\left|\phi_{\tau qi}\right|^2}\right)\phi_{\tau qi} + l_2\Delta\tau_{qi}, & \left|\phi_{\tau qi}\right| \geq \mu_{\tau q} \\ 0, & \left|\phi_{\tau qi}\right| < \mu_{\tau q} \end{cases},
\end{aligned} \tag{14}$$

where w_1, w_2, l_1, l_2 are positive constants; μ_q, $\mu_{\tau q}$ are small positive constants; and $g_{\tau qi} = s_{qi}\Delta_{\tau qi}/m_{qi}$.

Theorem 3. *Let $c_q > 0$, $2w_1 > w_2$, and $2l_1 > c_q + l_2$, under Assumptions 1–4, with the proposed constrained dynamic controller Eq. (13) and the anti-windup compensators Eq. (14), then it follows that s_{qi}, ϕ_{qi}, and $\phi_{\tau qi}$ are ultimately bounded. (The proof is given in Appendix C.)*

Let velocity command tracking error $e_{qi} = q_i - q_i^d$. It follows from Theorems 2 and 3 that $\left|e_{qi}\right| = \left|s_{qi} - \tilde{q}_i - \phi_{qi}\right| \leq \left|s_{qi}\right| + \left|\phi_{qi}\right| + \left|\tilde{q}_i\right|$, thus, e_{qi} is guaranteed to be ultimately bounded.

5. Stability analysis of the closed-loop system

Theorem 4. *Considering the switching topology $\bar{\mathcal{G}}_{\sigma(t)}$ and the formation tracking error system Eq. (5), under Assumptions 1–4, with the proposed formation protocol consisting of DO Eq. (6), CESO Eqs. ((7), (8), (9)), kinematic controller Eq. (12), and dynamic controller Eq. (13) with compensators Eq. (14), then it follows that the formation tracking error $\boldsymbol{e}_{pi}$ is ultimately bounded. (The proof is given in Appendix D.)*

6. Simulation results

The performance of the proposed formation protocol is evaluated in numerical simulation and compared to three state-of-the-art control methods. Moreover, two simulation examples are performed to substantiate the effectiveness of the proposed method on large-scale AUV swarm.

6.1. Simulation setup

The simulated experiments are conducted with a group of underactuated AUVs comprising one leader and six followers, with model parameters replicated from [36]. The constraints are enforced as $u_{\max} = -u_{\min} = 1.2$, $q_{\max} = r_{\max} = -q_{\min} = -r_{\min} = 0.4$, and $\tau_\rho^{\max} = -\tau_\rho^{\min} = 200$ $(\rho = u, q, r)$.

Table 2
Differences between the four methods compared in simulation.

	Positioning	Communication	Leader Info	Velocity Info	Guidance	Constraints	Ref.
Method 1	Relative	Switching Jointly	DO	CESO	Improved LOS	AC	–
Method 2	Relative	Switching	DO	CESO	Conventional LOS	RG	[16]
Method 3	Absolute	Static	Known	Measured	Sliding-based	–	[21]
Method 4	Relative	Static	Known	Measured	PP	–	[20]

Notations: DO = Distributed Observer; CESO = Cascaded Extended State Observer; LOS = Line-of-Sight;
AC = Anti-windup Compensator; RG = Reference Governor; PP = Prescribed Performance-based.

Table 3
Parameters of the proposed Method 1 (also partly utilized in Method 2).

Components	Parameters
DO Eq. (6)	$K_\eta = 15I_6$, $\kappa_1 = 8$, $\kappa_2 = 0.1$, $\varsigma = 7/9$
CESO Eqs. (7), (8), (9)	$k_{q1} = k_{r1} = 60$, $k_{q2} = k_{r2} = 1200$, $k_{q3} = k_{r3} = 8000$, $K_{p1} = 30I_3$, $K_{p2} = 300I_3$, $K_{p3} = 1000I_3$
LOS guidance law Eq. (10)	$\Delta_y = 4$
Kinematic law Eq. (12)	$b_x = b_\theta = b_\psi = 0.3$, $\xi = 2$, $w_n = 10$
Dynamic laws Eqs. (13) and (14)	$w_1 = 30$, $w_2 = 50$, $l_1 = 10$, $l_2 = 1e-5$, $c_\rho = 2$, $\mu_\rho = 0.01$, $\mu_{\tau\rho} = 1$, $(\rho = u, q, r)$

The trajectory of the leader is predefined as $\boldsymbol{p}_0(t) = \left[0.4t,\ 10 + 10\sin(\frac{\pi}{100}t),\ -20 + 10\sin(\frac{\pi}{100}t)\right]^T$, and the desired formation is specified as $\boldsymbol{h}_1 = [-4\cos(\pi/12)\cos(\pi/6),\ 4\cos(\pi/12)\sin(\pi/6),\ 4\sin(\pi/12)]^T$, $\boldsymbol{h}_2 = [-4\cos(\pi/12)\cos(2\pi/3),\ -4\cos(\pi/12)\sin(2\pi/3),\ -4\sin(\pi/12)]^T$, $\boldsymbol{h}_3 = 2\boldsymbol{h}_1$, $\boldsymbol{h}_4 = 2\boldsymbol{h}_2$, $\boldsymbol{h}_5 = 3\boldsymbol{h}_1$ and $\boldsymbol{h}_6 = 3\boldsymbol{h}_2$.

The initial positions of the followers are set away from the leader, as $\boldsymbol{p}_1(0) = [-10, 15, -5]^T$, $\boldsymbol{p}_2(0) = [5, 3, -5]^T$, $\boldsymbol{p}_3(0) = [5, 5, -5]^T$, $\boldsymbol{p}_4(0) = [-5, 0, -5]^T$, $\boldsymbol{p}_5(0) = [-10, -5, -5]^T$, $\boldsymbol{p}_6(0) = [-10, 2, -5]^T$. The initial orientations are set to zero. The dynamic uncertainties, consisting of second-order nonlinear hydrodynamic damping terms and environmental disturbances, are simulated as $\tau_{dui} = -d_{ui|ui|}\,|u_i|\,u_i + 0.2m_{ui}\sin(0.3t)$, $\tau_{dvi} = -d_{vi|vi|}\,|v_i|\,v_i + 0.05m_{vi}\sin(0.2t)$, $\tau_{dwi} = -d_{wi|wi|}\,|w_i|\,w_i + 0.05m_{wi}\sin(0.2t)$, $\tau_{dqi} = -d_{qi|qi|}\,|q_i|\,q_i + 0.2m_{qi}\sin(0.3t)$ and $\tau_{dri} = -d_{ri|ri|}\,|r_i|\,r_i + 0.2m_{ri}\sin(0.3t)$, where $d_{(\cdot)i|(\cdot)i|}$ are damping parameters. In order to test the robustness of the proposed method, certain variations are added to these damping terms, given by $d_{(\cdot)i|(\cdot)i|} = \{200, 133, 100, 80, 66, 57\}$.

The simulations are conducted in Matlab 2016b with the solver ode3(Bogacki–Shampine) and a fixed step size of 0.01s, on a PC with an Intel i5-7200 CPU, with 8 GB RAM, and running Win 10 64-bit OS.

6.2. Four methods for comparison

The proposed formation protocol (Method 1) is compared with three alternative protocols (Methods 2–4), as summarized in Table 2.

Method 1: The proposed formation protocol. The controller parameters used in the experiments are presented in Table 3. To test the performance under switching jointly connected networks, the communication topologies in the experiments switch between $\bar{\mathcal{G}}_1$, $\bar{\mathcal{G}}_2$, and $\bar{\mathcal{G}}_3$, according to signal $\sigma(t)$, as shown in Fig. 3.

Method 2: A distributed velocity-free tracking controller with conventional LOS guidance, incorporating a reference governor (RG) to address system constraints. The controller parameters used in the experiments are the same values as those used for Method 1, except for those of the RG, which are set according to [16]. The topologies in the experiments switch between $\bar{\mathcal{G}}_1 \bigcup \bar{\mathcal{G}}_2$ and $\bar{\mathcal{G}}_2 \bigcup \bar{\mathcal{G}}_3$, and each phase is active for 10 s.

Method 3: A centralized formation control approach [20], wherein each follower connects directly (and only) to the leader vehicle. This formation protocol was designed based on integral terminal sliding mode control. The parameters are tuned according to [20].

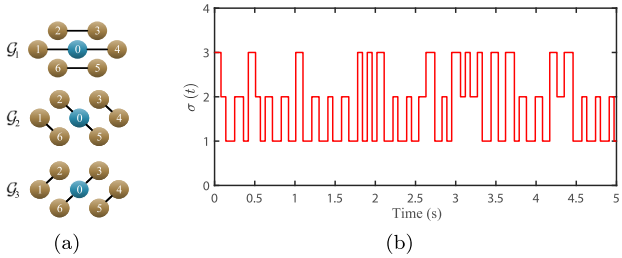

Fig. 3. Switching jointly connected communication topologies. (a) Three disconnected topologies. (b) Switching signal $\sigma(t)$.

Method 4: A distributed formation approach proposed in [21], wherein the controller was designed by concerning the prescribed transient and steady-state control performance. The controller parameters are tuned according to [21], and the topology is $\bar{\mathcal{G}}_1 \bigcup \bar{\mathcal{G}}_2$.

6.3. Results

The simulation results are presented in Figs. 4–10, where F_i $(i = 1, 2, \ldots, 6)$ is the ith follower. The control performance of the four methods is assessed according to maneuverability performance, tracking accuracy, and constraint satisfaction. Additionally, the estimation accuracies of the proposed DO and CESO in Method 1 are assessed, with a comparison to an existing DO from the literature.

Maneuverability performance: Fig. 4 shows the formation evolution of the AUV swarm under each method. Methods 1, 3, and 4 each achieve smooth formation maneuvers, while Method 2 leads to shaking. The observed difference between Methods 1 and 2 occurs because the conventional LOS guidance law in Method 2 has limited robustness against nonzero sideslip and attack angle, while the improved LOS guidance law in Method 1 achieves smoother maneuvers by introducing compensation terms.

Tracking accuracy: Fig. 5 shows the evolution of formation tracking errors e_{pi} under each method. The convergence rates of all methods are similar, with Methods 3 and 4 converging slightly more quickly (with Method 1 being slightly worse than Method 2). The zoom-in inserts show that Method 2 leads to noticeably larger steady state errors than the other methods and that Method 1 has the smallest steady state errors (slightly better than Methods 3 and 4).

In Table 4, tracking accuracy is also compared in terms of Integral Absolute Error (IAE), Integral Time Absolute Error (ITAE) for the entire evolution, and Root Mean Square Error (RMSE) for

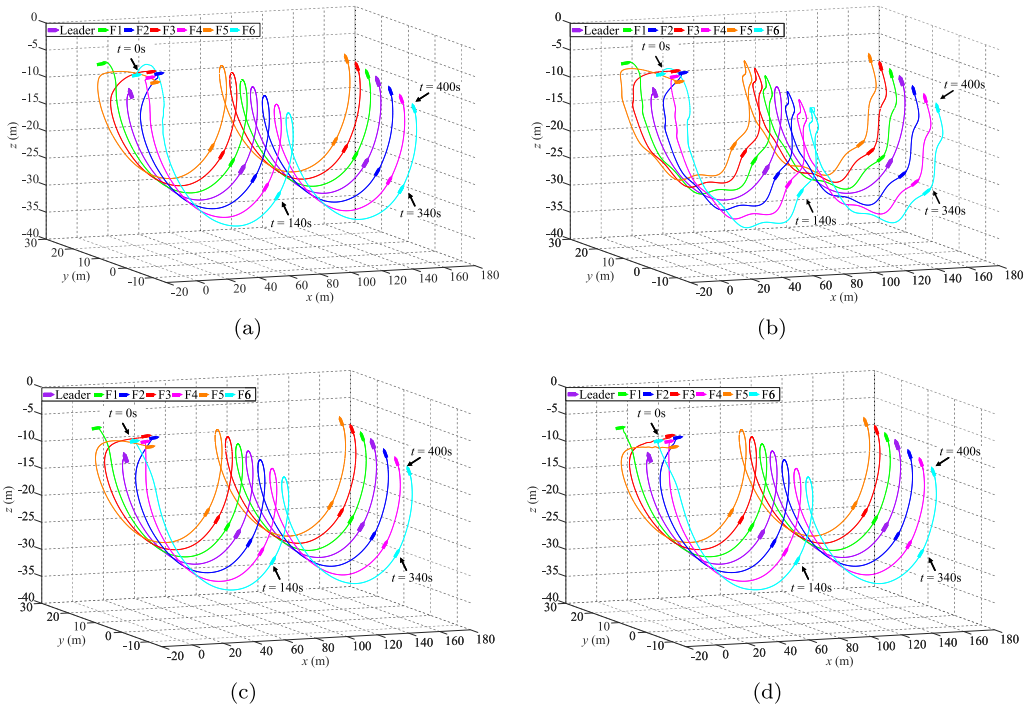

Fig. 4. Formation evolution of AUV swarm with (a) Method 1, (b) Method 2, (c) Method 3, and (d) Method 4.

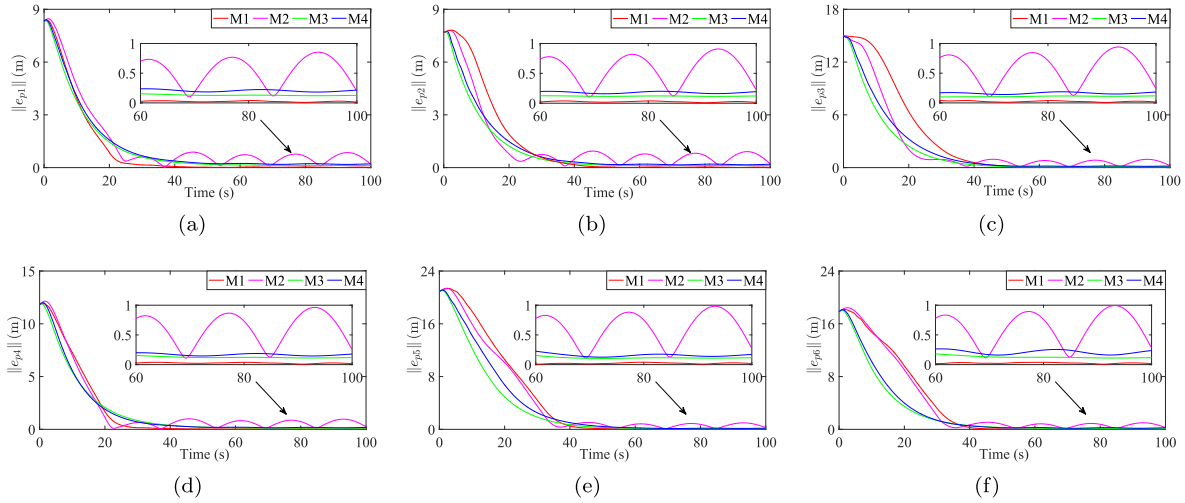

Fig. 5. Formation tracking error of Followers 1–6 (a–f) in the four methods.

Table 4
Performance comparison of the four methods.

*i*th AUV	IAE $= \int \|e_{pi}\| dt$ $(\times 10^2)$				ITAE $= \int t\|e_{pi}\| dt$ $(\times 10^4)$				RMSE $= (\int \|e_{pi}\|^2/T)^{0.5}$			
	M1	M2	M3	M4	M1	M2	M3	M4	M1	M2	M3	M4
1	**1.008**	2.991	1.462	1.804	**0.263**	4.207	1.088	1.724	**0.027**	0.569	0.125	0.204
2	1.340	2.952	**1.300**	1.623	**0.329**	4.435	1.029	1.544	**0.027**	0.603	0.119	0.182
3	3.096	4.136	**2.146**	2.620	**0.571**	4.680	1.088	1.572	**0.028**	0.624	0.116	0.171
4	**1.618**	3.600	1.872	2.023	**0.337**	4.715	1.067	1.38	**0.028**	0.637	0.116	0.16
5	4.519	6.188	**3.454**	4.090	**0.780**	5.163	1.239	1.641	**0.029**	0.649	0.114	0.156
6	3.824	5.726	**2.796**	3.192	**0.691**	5.143	1.156	1.693	**0.029**	0.656	0.115	0.188
AVG	2.567	4.266	**2.172**	2.559	**0.495**	4.7238	1.111	1.592	**0.028**	0.623	0.118	0.177

the steady phase. Method 3 has the lowest average IAE value, benefiting from its faster transient response. However, in the case of ITAE and RMSE, Method 1 preserves the lowest error values due to its minimal steady state errors. Method 2 has the highest error values for all three indicators.

Constraint satisfaction: The profiles of velocity and control inputs in the surge direction (i.e., u_i and τ_{ui} respectively) are given in Figs. 6 and 7. Methods 1 and 2 are capable of achieving velocity satisfaction, while both Methods 3 and 4 violate the velocity constraints at the initial stage, as seen in the zoom-in inserts

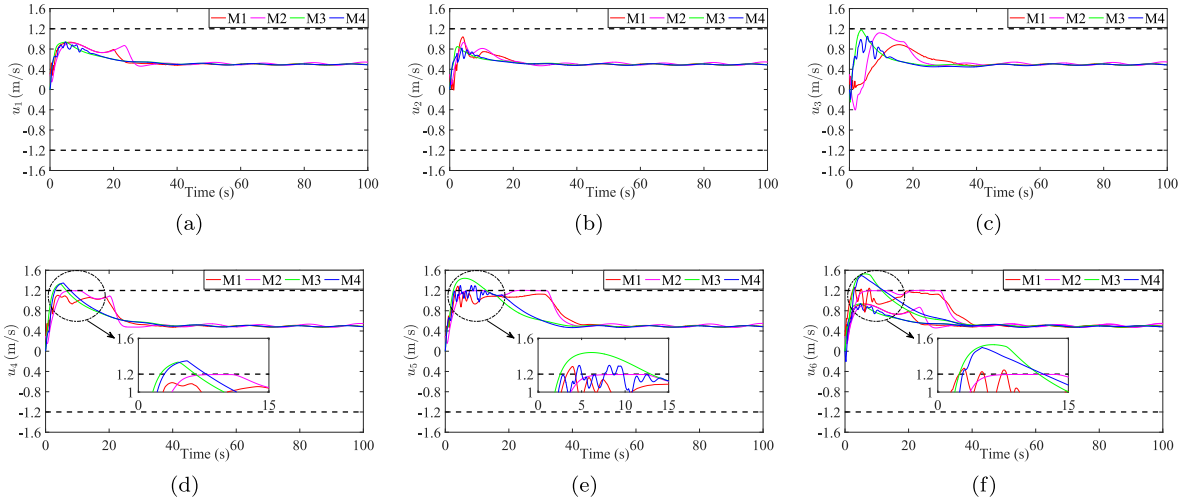

Fig. 6. Profile of surge velocity u_i of Followers 1–6 (a–f) in the four methods.

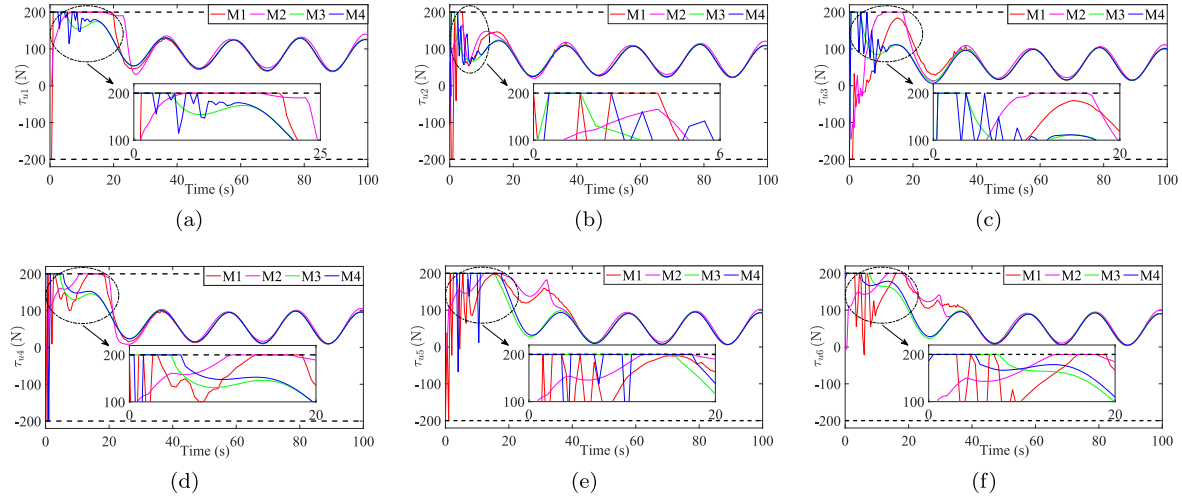

Fig. 7. Profile of surge input τ_{ui} of Followers 1–6 (a–f) in the four methods.

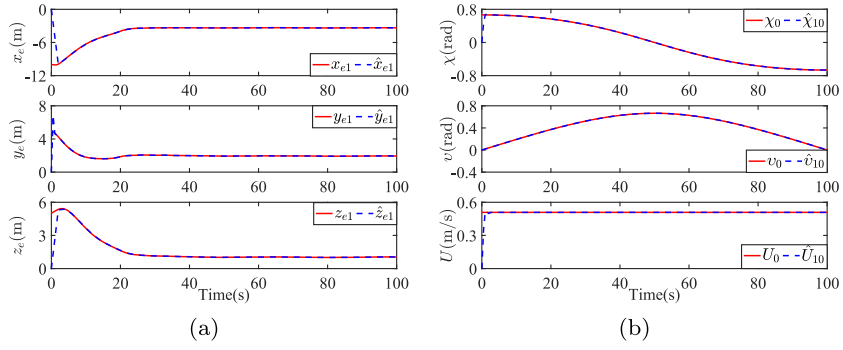

Fig. 8. Estimation result of the leader's information (a) $\boldsymbol{p}_{ei}$ and (b) $\boldsymbol{s}_0$ by Follower 1 using the proposed DO in Method 1.

in Fig. 6. This corresponds to Methods 3 and 4 having faster convergence rates than Methods 1 and 2. The input profiles in Fig. 7 show that the surge inputs in all four methods inevitably saturate due to the large initial tracking error.

Estimation accuracy: The estimation performance of the proposed DO in Method 1 is presented in Fig. 8. Using the DO of Method 1, the leader's information can be estimated by Follower 1 within a few seconds, so that the distributed estimation objective is achieved. For comparison, an existing DO [38] is also evaluated in Fig. 9, under the same topologies used in the experimental conditions of Method 1 (i.e., under switching jointly connected topologies). In Fig. 9, only the estimation signals of the first five seconds are provided, because these signals will diverge with t increasing. The DO of [38] deteriorates under a lack of topology connectivity, as might be present in underwater communications, while the proposed DO of Method 1 achieves

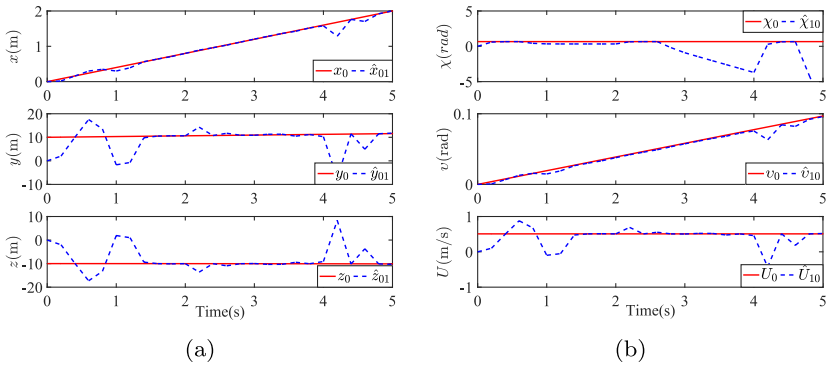

Fig. 9. Estimation result of leader's information (a) $\boldsymbol{p}_0$ and (b) $\boldsymbol{s}_0$ via DO in [38] under switching jointly connected topologies.

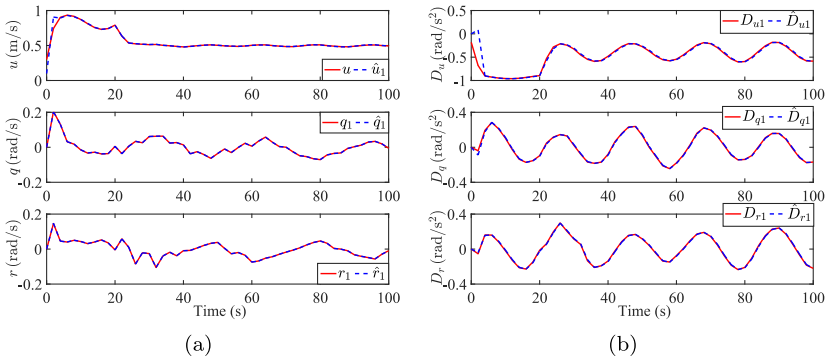

Fig. 10. Estimation result of (a) unmeasurable velocities and (b) unknown disturbances by Follower 1 via the proposed CESO in Method 1.

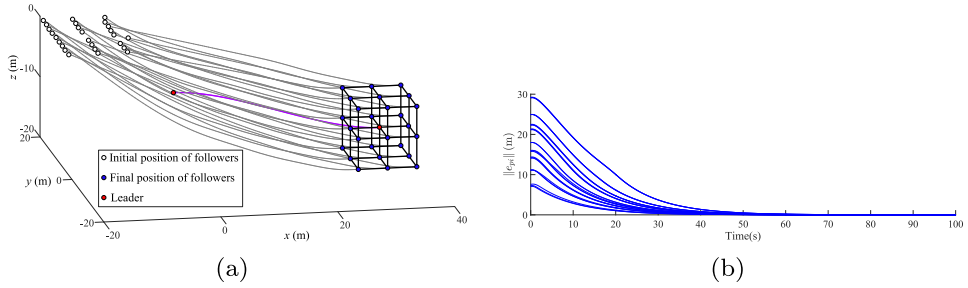

Fig. 11. Simulation with a robot swarm of 27 AUVs. (a) The trajectories of AUVs under the proposed formation protocol. (b) Formation tracking error of followers.

the estimation objective under the same conditions. Fig. 10 shows the estimation results of the proposed CESO in Method 1. It can be seen that the unmeasurable velocities and unknown disturbances can be precisely recovered, and therefore velocity sensors are not required.

6.4. Scalability of the proposed method

Scalability is an important advantage of distributed control strategies. In order to substantiate the scalability of our proposed protocol, we perform two simulations with larger robot swarms: a swarm of 27 AUVs and a swarm of 100 AUVs.

In the first scenario, the target formation is a cube with 27 nodes and 52 edges. The initial position and trajectory of the leader AUV are those defined in Section 6.1. The initial positions of the followers are distributed in a grid on the surface of the sea. As can be seen in Fig. 11(a), the target formation can be achieved within 100 s, and the formation tracking errors converge to the neighborhood around the origin, as presented in Fig. 11(b).

In the second scenario, the target formation is a cuboid with $5 \times 5 \times 4$ nodes and 235 edges. The initial positions of the followers are distributed in a 30 m radius circle around the leader. The leader moves straight forward, at a linear velocity of 0.5 m/s. The resulting trajectories of all followers in Fig. 12(a) show that our proposed formation control method can steer a swarm of one hundred AUVs to achieve the target formation. As can be seen in Fig. 12(b), which shows the formation tracking error of 25 arbitrary followers, the target formation can be achieved within 150 s and the formation tracking errors converge to the neighborhood around the origin.

We can notice that, in each scenario, the convergence rate is similar for all followers. This occurs because our proposed DO decomposes the formation control problem of the AUV swarm into decentralized trajectory tracking using local inter-AUV communication and local measurements. Thus, the convergence speed is mainly determined by the guidance-based kinematic control law, as discussed in Appendix D.

6.5. Discussion

The following conclusions can be drawn from the simulation results.

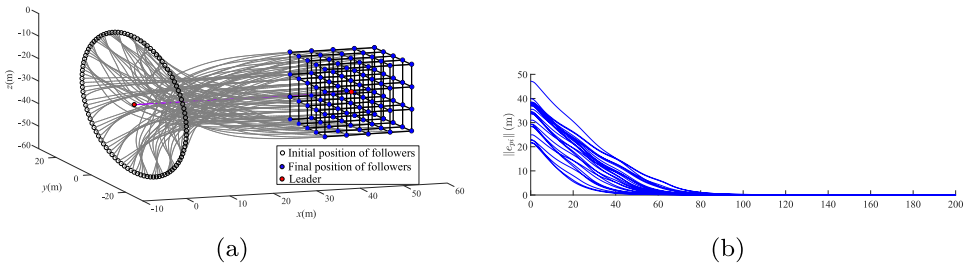

Fig. 12. Simulation with a robot swarm of 100 AUVs. (a) The trajectories of AUVs under the proposed formation protocol. (b) Formation tracking error of 25 arbitrary followers.

- Compared with Method 2, the proposed Method 1 guarantees smooth formation evolution and minimal steady state errors, which substantiates the improved performance of the proposed LOS guidance law in Method 1.
- Compared with Methods 3 and 4, the proposed Method 1 performs better in terms of steady state errors and constraint satisfaction. In addition, the proposed CESO in Method 1 removes dependence on velocity sensors and the assumption of static topologies, which cannot be guaranteed in practice.
- Compared with the existing DO in [38], Method 1 is verified to be applicable under switching jointly connected topologies. The proposed DO in Method 1 removes dependence on the common assumption of constant connectivity, which cannot be guaranteed in practice.

It can be concluded that the proposed formation protocol is proved to have the desired maneuverability performance, improved tracking accuracy, and guaranteed constraint satisfaction, in comparison to the state of the art. Moreover, the proposed DO and CESO handle several practical constraints for formation control of underactuated AUVs that have not previously been fully considered: switching jointly connected topologies and unavailable velocity measurements. Regarding scalability and large-scale swarms, it should be noted that the simulation experiments in this research were performed in an ideal environment. For instance, time delays of communication techniques in real oceanic environments are not considered, but are inevitable in practice. In addition, collision avoidance is an important issue for large-scale robot swarms, posing substantial challenges in formation achievement and maintenance. Addressing these challenges for deployment of large-scale AUV swarms will require future research or extensions, for instance using multi-leader protocols.

Remark 9. This research firstly defines some of the research gaps in formation control of AUV swarms by classifying existing approaches in terms of topology, measurements, constraints, and dimensions, as shown in Table 1. Secondly, this research proposes a formation protocol that addresses each of the defined gaps, then assesses the proposed method in comparative simulations, in terms of maneuverability performance, tracking accuracy, constraint satisfaction, and estimation accuracy. Quantitative factors, including IAE, ITAE and RMSE, are employed in the assessment.

7. Conclusion

This paper addresses distributed formation control of underactuated AUVs moving in 3D space and subject to switching jointly connected topologies, unmeasurable velocities, and system constraints. A hybrid formation protocol that incorporates aspects of both centralized and decentralized control is proposed such that the objectives of distributed estimation and geometric convergence are achieved. The notable features of the proposed method can be summarized as follows. Firstly, the proposed method uses decentralized control in the sense that it assumes access to only local communication and local sensing, and therefore can be promoted to large-scale AUV swarms. Secondly, there is potential for wide real-world applicability, as the method does not have to rely on velocity sensing, and can instead make use of any relative positioning technology [12]. Thirdly, limitations in practice, such as switching but occasionally disconnected topologies, external uncertainties, and system constraints, have been comprehensively considered in the proposed formation protocol. The comparative simulation results substantiate the effectiveness of the proposed method and its improvements over the state of the art. Future work will still be required for practical deployments of large-scale AUV swarms, including collision avoidance and management of time delays. In addition, real experiments are still rare in multi-AUV research in general. It is of great importance that the community begin implementing state-of-the-art theoretical contributions on real AUVs to be verified in real environments.

Declaration of competing interest

The authors declare that they have no known competing financial interests or personal relationships that could have appeared to influence the work reported in this paper.

Acknowledgments

This work is supported by the National Key R&D Program of China (Grant No. 2021YFB2011300), the National Science and Technology Major Project (Grant No. 2017-V-0010-0060), the National Natural Science Foundation of China (Grants No. 51620105010 and 51675019), the National Basic Research Program of China (Grant No. JCKY2018601C107), the fellowship of China Postdoctoral Science Foundation (Grant No. 2022M710305), and the State Key Laboratory of Software Development Environment. Mary Katherine Heinrich and Marco Dorigo acknowledge support from the Belgian F.R.S.-FNRS, of which they are a Postdoctoral Researcher and a Research Director respectively.

Appendix A. Proof of Theorem 1

First, take note of the following two lemmas.

Lemma 2 ([43]). *A continuous positive definite function $V(t)$ is finite-time stable at the origin if there exist positive constants $\rho_1 > 0$, $\rho_2 > 0$, and $0 < c < 1$, such that $\dot{V}(t) \leq -\rho_1 V(t) - \rho_2 V^c(t)$, $t \geq t_0$, and the settling time is given by $T_f \leq T_0 + \frac{1}{\rho_1(1-c)} \ln \frac{\rho_1 V^{1-c}(T_0)+\rho_2}{\rho_2}$.*

Lemma 3 ([44]). *Consider a group of systems $\dot{\boldsymbol{x}}(t) = \boldsymbol{f}_\sigma(\boldsymbol{x}), \boldsymbol{f}_\sigma(\boldsymbol{0}) = \boldsymbol{0}, \boldsymbol{x} \in \mathbb{R}^n$, where $\sigma : [0, \infty) \to \{1, 2, \ldots, M\}$ is a piecewise constant function of time, $\boldsymbol{f}_i$ is a continuous function with respect*

to $\boldsymbol{x}$ for any fixed index $i \in \{1, 2, \ldots, M\}$. If the switched system is asymptotically stable and $\dot{\boldsymbol{x}}(t) = \boldsymbol{f}_i(\boldsymbol{x})$ is finite-time stable for any fixed i, then system is finite-time stable.

Proof. Let $\boldsymbol{\mu}_\eta = \left[\boldsymbol{\mu}_{\eta 1}^T, \boldsymbol{\mu}_{\eta 2}^T, \ldots, \boldsymbol{\mu}_{\eta N}^T\right]^T$ and $\tilde{\boldsymbol{\eta}}_0 = \left[\tilde{\boldsymbol{\eta}}_{10}^T, \tilde{\boldsymbol{\eta}}_{20}^T, \ldots, \tilde{\boldsymbol{\eta}}_{N0}^T\right]^T$. It follows that $\boldsymbol{\mu}_\eta(t) = \boldsymbol{P}_{\sigma(t)}\tilde{\boldsymbol{\eta}}_0(t)$, where $\boldsymbol{P}_{\sigma(t)} = \left(\boldsymbol{H}_{\sigma(t)} \otimes \boldsymbol{I}_6\right)$. Consider Lyapunov function $V_\eta = \boldsymbol{\mu}_\eta^T\boldsymbol{\mu}_\eta/2$, which is continuously differentiable at any non-switching instant. Following Lemma 3, the proof will be presented in two steps.

Step 1: We will show that $\tilde{\boldsymbol{\eta}}_0$ is asymptotically stable at the origin. Firstly, assume that graph $\bar{\mathcal{G}}_q$ is active at non-switching time t. Differentiating $\boldsymbol{\mu}_{\eta i}$ and substituting Eq. (6) yields $\dot{\boldsymbol{\mu}}_{\eta i} = -\boldsymbol{K}_\eta\boldsymbol{\mu}_{\eta i} + \dot{\boldsymbol{\Phi}}_{\eta i} - \kappa_1 \mathrm{sgn}\left(\boldsymbol{\mu}_{\eta i}\right) - \kappa_2\boldsymbol{\mu}_{\eta i}^{\varsigma}$ if $\alpha_i > 0$, and $\dot{\boldsymbol{\mu}}_{\eta i} = \boldsymbol{0}$ if $\alpha_i = 0$.

Note that $\alpha_i = 0$ is equivalent to $i \notin C(q)$ [32]. Therefore, taking the time derivative of V_η yields

$$\begin{aligned}\dot{V}_\eta &= \sum_{i\in C(q)} -\boldsymbol{\mu}_{\eta i}^T\boldsymbol{K}_\eta\boldsymbol{\mu}_{\eta i} + \boldsymbol{\mu}_{\eta i}^T\dot{\boldsymbol{\Phi}}_{\eta i} - \kappa_1\left|\boldsymbol{\mu}_{\eta i}\right| - \kappa_2|\boldsymbol{\mu}_{\eta i}|^{1+\varsigma} \\ &\le \sum_{i\in C(q)} -\boldsymbol{\mu}_{\eta i}^T\boldsymbol{K}_\eta\boldsymbol{\mu}_{\eta i} - (\kappa_1 - \gamma_\Phi)\left|\boldsymbol{\mu}_{\eta i}\right| - \kappa_2(\boldsymbol{\mu}_{\eta i}^T\boldsymbol{\mu}_{\eta i})^{\frac{\varsigma+1}{2}} \\ &\le -\lambda_{\min}\left(\boldsymbol{K}_\eta\right)\sum_{i\in C(q)}\boldsymbol{\mu}_{\eta i}^T\boldsymbol{\mu}_{\eta i} \le 0,\end{aligned} \tag{A.1}$$

where we use the fact that $|\boldsymbol{\mu}_{\eta i}|^{2(\varsigma+1)} \ge (\boldsymbol{\mu}_{\eta i}^T\boldsymbol{\mu}_{\eta i})^{\varsigma+1}$ in the first inequality (based on Lemma 2 in [43]). Eq. (A.1) implies that $\lim_{t\to\infty} V_\eta(t)$ exists.

Secondly, it is shown that $\lim_{t\to\infty}\boldsymbol{\mu}_\eta(t) = \boldsymbol{0}$. Considering the infinite sequences $V_\eta(t_k), k = 0, 1, \ldots$, and recalling Cauchy's convergence criteria, it can be derived that for any $\varepsilon > 0$, there exists a positive integer k_ε such that, for $\forall k > k_\varepsilon$, $\left|V_\eta(t_{k+1}) - V_\eta(t_k)\right| < \varepsilon$, i.e., $\int_{t_k}^{t_{k+1}} -\dot{V}_\eta(t)\,dt < \varepsilon$. This can be rewritten into the following sum of integrals $\sum_{l=0}^{l_k-1}\int_{t_k^l}^{t_k^{l+1}} -\dot{V}_\eta(t)\,dt < \varepsilon$. For each integral, following Eq. (A.1) yields that

$$\begin{aligned}\int_{t_k^l}^{t_k^{l+1}} -\dot{V}_\eta(t)\,dt &\ge \int_{t_k^l}^{t_k^{l+1}} \lambda_{\min}\left(\boldsymbol{K}_\eta\right)\sum_{i\in C\left(\sigma\left(t_k^l\right)\right)}\boldsymbol{\mu}_{\eta i}^T\boldsymbol{\mu}_{\eta i}dt \\ &\ge \lambda_{\min}\left(\boldsymbol{K}_\eta\right)\int_{t_k^l}^{t_k^l+\tau}\sum_{i\in C\left(\sigma\left(t_k^l\right)\right)}\boldsymbol{\mu}_{\eta i}^T\boldsymbol{\mu}_{\eta i}dt\end{aligned}. \tag{A.2}$$

Thus, $\lim_{t\to\infty}\int_t^{t+\tau}\sum_{l=0}^{l_k-1}\sum_{i\in C\left(\sigma\left(t_k^l\right)\right)}\boldsymbol{\mu}_{\eta i}^T(s)\,\boldsymbol{\mu}_{\eta i}(s)ds = 0$. Due to the joint connectivity of the graph during $[t_k, t_{k+1})$, Lemma 1 implies that $\lim_{t\to\infty}\int_t^{t+\tau}\sum_{i=1}^N a_i\boldsymbol{\mu}_{\eta i}^T(s)\,\boldsymbol{\mu}_{\eta i}(s)\,ds = 0$, where a_i $(i = 1, \ldots, N)$ are some positive constants. Following Eq. (A.1), $\boldsymbol{\mu}_\eta(t)$ are uniformly bounded, and thus $\dot{\boldsymbol{\mu}}_\eta(t)$ is bounded. Thus, $\boldsymbol{\mu}_\eta^T\boldsymbol{\mu}_\eta$ is uniformly continuous. Applying Barbalat's Lemma, it can be derived that $\lim_{t\to\infty}\boldsymbol{\mu}_\eta(t) = \boldsymbol{0}$.

Thirdly, it will show that $\lim_{t\to\infty}\tilde{\boldsymbol{\eta}}_0(t) = \boldsymbol{0}$. Without loss of generality, consider only the first element of $\boldsymbol{\mu}_{\eta i}$ and $\tilde{\boldsymbol{\eta}}_{i0}$ in the proof, denoted by $\boldsymbol{\mu}_{\eta i}^x$ and $\tilde{\boldsymbol{\eta}}_{i0}^x$. Let $\boldsymbol{\mu}_\eta^x = \left[\boldsymbol{\mu}_{\eta 1}^x, \boldsymbol{\mu}_{\eta 2}^x, \ldots, \boldsymbol{\mu}_{\eta N}^x\right]^T$ and $\tilde{\boldsymbol{\eta}}_0^x = \left[\tilde{\boldsymbol{\eta}}_{10}^x, \tilde{\boldsymbol{\eta}}_{20}^x, \ldots, \tilde{\boldsymbol{\eta}}_{N0}^x\right]^T$. Thus, $\boldsymbol{\mu}_\eta^x = \boldsymbol{H}_{\sigma(t)}\tilde{\boldsymbol{\eta}}_0^x$. Assume that the jointly connected graph across $[t_k, t_{k+1})$ is denoted by $\bar{\mathcal{G}}_k$. Due to the symmetry of $\boldsymbol{H}_k$, there exists an orthogonal matrix $\boldsymbol{U}_k$, such that $\boldsymbol{U}_k\boldsymbol{H}_k\boldsymbol{U}_k^T = \boldsymbol{\Lambda}_k = \mathrm{diag}\left\{\lambda_k^{i_1}, \lambda_k^{i_2}, \ldots, \lambda_k^{i_N}\right\}$, where $\lambda_q^{i_1}, \lambda_k^{i_2}, \ldots, \lambda_k^{i_N}$ are the N eigenvalues of $\boldsymbol{H}_k$, $i_1, i_2, \ldots, i_N$ and form a permutation of $1, 2, \ldots, N$. Let $\boldsymbol{\varepsilon} = \boldsymbol{U}_q\tilde{\boldsymbol{\eta}}_0^x$, then $\left(\tilde{\boldsymbol{\eta}}_0^x\right)^T\boldsymbol{\mu}_\eta^x = \left(\tilde{\boldsymbol{\eta}}_0^x\right)^T\boldsymbol{H}_k\tilde{\boldsymbol{\eta}}_0^x = \boldsymbol{\varepsilon}^T\boldsymbol{\Lambda}_k\boldsymbol{\varepsilon} \ge \delta_{\min}\sum_{i\in C\left(\sigma\left(t_k^l\right)\right)}\varepsilon_i^2 \ge 0$, where $l = 0, 1, \ldots, l_k - 1$ and $\delta_{\min} = \min\left\{\lambda_{\min}\left(\boldsymbol{H}_q\right) | q \in \mathcal{Q}\right\}$. Following from the joint connectivity, Lemma 1, and $\lim_{t\to\infty}\mu_\eta^x(t) = \boldsymbol{0}$, it can be inferred that $\lim_{t\to\infty}\sum_{l=0}^{l_k-1}\sum_{i\in C\left(\sigma\left(t_k^l\right)\right)}\varepsilon_i^2 = \lim_{t\to\infty}\sum_{i=1}^N a_i\varepsilon_i^2 = 0$. This implies that $\lim_{t\to\infty}\sum_{i=1}^N\varepsilon_i = 0$, i.e., $\lim_{t\to\infty}\tilde{\boldsymbol{\eta}}_0^x = \boldsymbol{0}$. Thus, it can be concluded that $\lim_{t\to\infty}\tilde{\boldsymbol{\eta}}_0(t) = \boldsymbol{0}$.

Step 2: We will show that, for a fixed index $q \in \mathcal{Q}$, the estimation error $\tilde{\boldsymbol{\eta}}_{i0}$ is finite-time stable. Note that the switching topologies are jointly connected, and the ith follower cannot always be isolated. In other words, there exists at least one graph $\bar{\mathcal{G}}_{q'}$ with $q' \in \mathcal{Q}$ such that $\alpha_i > 0$. Thus, we consider the Lyapunov function candidate $V_{\eta i} = \boldsymbol{\mu}_{\eta i}^T\boldsymbol{\mu}_{\eta i}/2$ under graph $\bar{\mathcal{G}}_{q'}$. Following Eq. (A.1), the derivative is given by $\dot{V}_{\eta i} \le -\boldsymbol{\mu}_{\eta i}^T\boldsymbol{K}_\eta\mu_{\eta i} - (\kappa_1 - \gamma_\Phi)\left|\boldsymbol{\mu}_{\eta i}\right| - \kappa_2\left(\boldsymbol{\mu}_{\eta i}^T\boldsymbol{\mu}_{\eta i}\right)^{\frac{\varsigma+1}{2}} \le -\lambda_{\min}\left(\boldsymbol{K}_\eta\right)V_{\eta i} - \kappa_2 2^{\frac{\varsigma+1}{2}}V_{\eta i}^{\frac{\varsigma+1}{2}}$. It follows from Lemma 2 that $\boldsymbol{\mu}_{\eta i} \to 0$ in finite time $T_{fi} \le T_0 + \frac{2}{\lambda_{\min}\left(\boldsymbol{K}_\eta\right)(1-\varsigma)}\ln\frac{\lambda_{\min}\left(\boldsymbol{K}_\eta\right)2^{-\frac{\varsigma+1}{2}}V_{\eta i}^{\frac{\varsigma+1}{2}}(T_0)+\kappa_2}{\kappa_2}$. The remaining proof is similar to that of Step 1. According to Lemma 3, we can conclude that the estimation error $\tilde{\boldsymbol{\eta}}_0$ converges to zero in finite time. ■

Appendix B. Proof of Theorem 2

Proof. Step 1: Let $\boldsymbol{\pi}_{qi} = \left[\tilde{\theta}_i, \tilde{q}_i, \tilde{D}_{qi}\right]^T$. It follows from Eqs. (1), (2), and (7) that $\dot{\boldsymbol{\pi}}_{qi} = \boldsymbol{L}_q\boldsymbol{\pi}_{qi} + \boldsymbol{N}_{qi}$, where $\boldsymbol{L}_q = \begin{pmatrix}-k_{q1} & 1 & 0\\ -k_{q2} & 0 & 1\\ -k_{q3} & 0 & 0\end{pmatrix}$ and $\boldsymbol{N}_{qi} = \left[0, 0, -\dot{D}_{qi}\right]^T$. The stability of the error dynamics is guaranteed if there exist a positive definite matrix $\boldsymbol{Q}_q \in \mathbb{R}^{3\times3}$ and a positive constant $\epsilon_q > 1$ such that $\boldsymbol{L}_q^T\boldsymbol{Q}_q + \boldsymbol{Q}_q\boldsymbol{L}_q \le -\epsilon_q\boldsymbol{I}_3$.

Consider the Lyapunov function $V_{qi} = \boldsymbol{\pi}_{qi}^T\boldsymbol{Q}_q\boldsymbol{\pi}_{qi}$, with its derivative as $\dot{V}_{qi} = \boldsymbol{\pi}_{qi}^T\left(\boldsymbol{L}_q^T\boldsymbol{Q}_q + \boldsymbol{Q}_q\boldsymbol{L}_q\right)\boldsymbol{\pi}_{qi} + 2\boldsymbol{\pi}_{qi}^T\boldsymbol{Q}_q\boldsymbol{N}_{qi} \le -\epsilon_q\boldsymbol{\pi}_{qi}^T\boldsymbol{\pi}_{qi} + 2\left\|\boldsymbol{\pi}_{qi}\right\|\left\|\boldsymbol{Q}_q\right\|\left\|\boldsymbol{N}_{qi}\right\| \le -\left\|\boldsymbol{\pi}_{qi}\right\|\left(\epsilon_q\left\|\boldsymbol{\pi}_{qi}\right\| - 2\left\|\boldsymbol{Q}_q\right\|\bar{N}_q\right)$. It can then be derived that $\left\|\boldsymbol{\pi}_{qi}\right\| \le 2\left\|\boldsymbol{Q}_q\right\|\bar{N}_q/\epsilon_q$ and that the upper bound can be decreased by choosing appropriate parameters. **Step 2:** Define $\boldsymbol{\pi}_{ri} = \left[\tilde{\xi}_{ri}, \tilde{r}_i, \tilde{D}_{ri}\right]^T$, where $\tilde{\xi}_{ri} = \hat{\xi}_{ri} - \xi_{ri}$. It can then be deduced that $\dot{\boldsymbol{\pi}}_{ri} = \boldsymbol{L}_r\boldsymbol{\pi}_{ri} + \boldsymbol{N}_{ri}$, where $\boldsymbol{L}_r = \begin{pmatrix}-k_{r1} & 1 & 0\\ -k_{r2} & 0 & 1\\ -k_{r3} & 0 & 0\end{pmatrix}$ and $\boldsymbol{N}_{ri} = \left[-\tilde{q}_i\psi_i\sin\theta_i, 0, -\dot{D}_{ri}\right]^T$. Step 1 and Assumption 2 guarantee the boundedness of $\|\boldsymbol{N}_{ri}\|$. Analogously to Step 1, $\|\boldsymbol{\pi}_{ri}\|$ will also be bounded.

Step 3: Define $\boldsymbol{\pi}_{pi} = \left[\tilde{\boldsymbol{\xi}}_{pi}, \tilde{\boldsymbol{v}}_{B_i}, \tilde{\boldsymbol{D}}_{pi}\right]^T$, where $\tilde{\boldsymbol{\pi}}_{pi} = \hat{\boldsymbol{\pi}}_{pi} - \boldsymbol{\pi}_{pi}$. The following can then be obtained: $\dot{\boldsymbol{\pi}}_{pi} = \boldsymbol{L}_p\boldsymbol{\pi}_{pi} + \boldsymbol{N}_{pi}$, where $\boldsymbol{L}_p = \begin{pmatrix}-\boldsymbol{K}_{p1} & \boldsymbol{I}_3 & 0\\ -\boldsymbol{K}_{p2} & 0 & \boldsymbol{I}_3\\ -\boldsymbol{K}_{p3} & 0 & 0\end{pmatrix}$ and $\boldsymbol{N}_{pi} = \left[\boldsymbol{g}_{pi}, \boldsymbol{0}, -\dot{\boldsymbol{D}}_{pi}\right]^T$, where $\boldsymbol{g}_{pi} = \boldsymbol{S}_I^{B_i}\left(\hat{r}_i, \hat{q}_i, \theta_i\right)\boldsymbol{\xi}_{pi}^e - \boldsymbol{S}_I^{B_i}\left(r_i, q_i, \theta_i\right)\boldsymbol{\xi}_{pi} - \boldsymbol{R}_I^{B_i}\left(\dot{\boldsymbol{p}}_0^e - \dot{\boldsymbol{p}}_0\right)$. From Theorem 1, it follows that $\lim_{t\to\infty}\boldsymbol{\xi}_{pi}^e(t) - \boldsymbol{\xi}_{pi}(t) = \boldsymbol{0}$ and $\lim_{t\to\infty}\dot{\boldsymbol{p}}_0^e(t) - \dot{\boldsymbol{p}}_0(t) = \boldsymbol{0}$. The ultimate boundedness of $\boldsymbol{S}_I^{B_i}\left(\hat{r}_i, \hat{q}_i, \theta_i\right) - \boldsymbol{S}_I^{B_i}\left(r_i, q_i, \theta_i\right)$ can then also be proven, according to the former steps. It follows that there exists a positive constant $\bar{N}_p$ such that $\left\|\boldsymbol{N}_{pi}\right\| \le \bar{N}_p$. The remainder of the proof for Step 3 is omitted here, as it can be inferred from Step 1. ■

Appendix C. Proof of Theorem 3

Proof. From Eq. (7), the dynamic model of $\hat{q}_i$ can be expressed as $\dot{\hat{q}}_i = -k_{q2}\tilde{\theta}_i + \left(\tau_{qi} + \Delta\tau_{qi}\right)/m_{qi} + \hat{D}_{qi}$. Then, differentiating s_{qi} yields

$\dot{s}_{qi} = -c_q s_{qi} + c_q \phi_{\tau qi} - k_{q2}\tilde{\theta}_i + \Delta\tau_{qi}/m_{qi}$. Consider the Lyapunov candidate $V_{qi} = s_{qi}^2/2 + \phi_{qi}^2/2 + \phi_{\tau qi}^2/2$. Differentiating V_{ui} yields

$$\begin{aligned}\dot{V}_{qi} = &-c_q s_{qi}^2 + c_q s_{qi}\phi_{\tau qi} - k_{q2} s_{qi}\tilde{\theta}_i + g_{\tau qi} - w_1\phi_{qi}^2 \\ &- w_2\Delta q_i^2/2 + w_2\phi_{qi}\Delta q_i \\ &- l_1\phi_{\tau qi}^2 - \left|g_{\tau qi}\right| - l_2\Delta\tau_{qi}^2/2 + l_2\phi_{\tau qi}\Delta\tau_{qi}.\end{aligned} \tag{C.1}$$

Recall the existence of the inequalities $2s_{qi}\phi_{\tau qi} \le s_{qi}^2 + \phi_{\tau qi}^2$, $2\phi_{qi}\Delta q_i \le \phi_{qi}^2 + \Delta q_i^2 m$, $2\phi_{\tau qi}\Delta\tau_{qi} \le \phi_{\tau qi}^2 + \Delta\tau_{qi}^2$. It then follows that Eq. (C.1) can be reorganized as

$$\begin{aligned}\dot{V}_{qi} \le &-c_q e_{ui}^2/2 - (2w_1 - w_2)\,\phi_{ui}^2/2 - \left(2l_1 - c_q - l_2\right)\phi_{\tau ui}^2/2 \\ &- k_{q2} s_{qi}\tilde{\theta}_i,\end{aligned} \tag{C.2}$$

where the parameters are chosen such that $c_q > 0$, $2w_1 > w_2$ and $2l_1 > c_q + l_2$. After defining $\boldsymbol{E}_{qi} = \left[s_{qi}, \phi_{qi}, \phi_{\tau qi}\right]^T$, Eq. (C.2) can then be rewritten as $\dot{V}_{qi} \le -\boldsymbol{E}_{qi}^T\boldsymbol{K}_q\boldsymbol{E}_{qi} + \boldsymbol{E}_{qi}^T\boldsymbol{T}_{qi} \le -\left\|\boldsymbol{E}_{qi}\right\|\left(\left\|\boldsymbol{K}_q\right\|\left\|\boldsymbol{E}_{qi}\right\| - \left\|\boldsymbol{T}_{qi}\right\|\right)$, where $\boldsymbol{K}_q = diag\left(c_q/2, w_1 - w_2/2, l_1 - \left(c_q + l_2\right)/2\right)$ and $\boldsymbol{T}_{ui} = \left[-k_{q2}\tilde{\theta}_i, 0, 0\right]^T$. Theorem 2 implies that $\left\|\boldsymbol{T}_{qi}\right\| \le \bar{T}_{qi}$, with $\bar{T}_{qi} > 0$. It can therefore be concluded that $\left\|\boldsymbol{E}_{qi}\right\| \le \bar{T}_{qi}/\lambda_{\min}\left(\boldsymbol{K}_q\right)$. ■

Appendix D. Proof of Theorem 4

Proof. Step 1: After defining angle tracking error $\boldsymbol{e}_{ai} = \left[e_{\theta i}, e_{\psi i}\right]^T = \left[\theta_i - \theta_i^d, \psi_i - \psi_i^d\right]^T$, it can be proven that $\boldsymbol{e}_{ai}$ is ultimately bounded. When considering Lyapunov function candidate $V_{ai} = \boldsymbol{e}_{ai}^T\boldsymbol{e}_{ai}/2$, differentiating V_{ai} with respect to time yields $\dot{V}_{ai} = e_{\theta i}\left(-b_\theta e_{\theta i} + e_{qi}\right) + e_{\psi i}\left(-b_\psi e_{\psi i} + e_{ri}/\cos\theta_i\right) = -\boldsymbol{e}_{ai}^T\boldsymbol{L}_a\boldsymbol{e}_{ai} + \boldsymbol{e}_{ai}^T\boldsymbol{M}_{ai}$, where $e_{qi} = q_i - q_i^d$, $e_{ri} = r_i - r_i^d$, $\boldsymbol{L}_a = \begin{pmatrix} b_\theta & 0 \\ 0 & b_\psi \end{pmatrix}$ and $\boldsymbol{M}_{ai} = \left[e_{qi}, e_{ri}/\cos\theta_i\right]^T$. Under Theorem 3, $\left\|\boldsymbol{M}_{ai}\right\|$ is bounded by a positive constant denoted by $\bar{M}_{ai}$. It therefore follows that $\left\|\boldsymbol{e}_{ai}\right\| \le \bar{M}_{ai}/\lambda_{\min}\left(\boldsymbol{L}_a\right)$.

Step 2: The ultimate boundedness of $\boldsymbol{e}_{pi}$ is given as follows. Consider Lyapunov function candidate $V_{pi} = \boldsymbol{e}_{pi}^T\boldsymbol{e}_{pi}/2$ and differentiating V_{pi} along Eq. (5), it yields that

$$\begin{aligned}\dot{V}_{pi} = &\, e_{xi}\left(U_i\cos\psi_{ei}\cos\theta_{ei} - U_0 + f_{xi}\right) + e_{yi}\left(U_i\sin\psi_{ei}\cos\theta_{ei} + f_{yi}\right) \\ &+ e_{zi}\left(-U_i\sin\theta_{ei} + f_{zi}\right).\end{aligned} \tag{D.1}$$

Then, note that $\boldsymbol{R}_{B_i}^F\left(\psi_{ei}, \theta_{ei}\right) - \boldsymbol{R}_{B_i}^F\left(\psi_{ei}^d, \theta_{ei}^d\right) = \left(\boldsymbol{R}_F^I\left(\chi_0, \upsilon_0\right)\right)^T\boldsymbol{R}_{B_i}^I\left(\psi_i, \theta_i\right) - \left(\boldsymbol{R}_F^I\left(\hat{\chi}_{i0}, \hat{\upsilon}_{i0}\right)\right)^T\boldsymbol{R}_{B_i}^I\left(\psi_i^d, \theta_i^d\right) = \left(\boldsymbol{R}_F^I\left(\chi_0, \upsilon_0\right)\right)^T\left(\boldsymbol{R}_{B_i}^I\left(\psi_i, \theta_i\right) - \boldsymbol{R}_{B_i}^I\left(\psi_i^d, \theta_i^d\right)\right) + \left(\boldsymbol{R}_F^I\left(\chi_0, \upsilon_0\right) - \boldsymbol{R}_F^I\left(\hat{\chi}_{i0}, \hat{\upsilon}_{i0}\right)\right)^T\boldsymbol{R}_{B_i}^I\left(\psi_i^d, \theta_i^d\right)$. Under Theorem 1 and Step 1, $\boldsymbol{R}_{B_i}^F\left(\psi_{ei}, \theta_{ei}\right) - \boldsymbol{R}_{B_i}^F\left(\psi_{ei}^d, \theta_{ei}^d\right)$ converge to a small neighborhood of zero. Then, one has

$$\begin{aligned}&\cos\psi_{ei}\cos\theta_{ei} - \cos\psi_{ei}^d\cos\theta_{ei}^d \le e_{Rx}, \sin\psi_{ei}\cos\theta_{ei} - \sin\psi_{ei}^d\cos\theta_{ei}^d \\ &\le e_{Ry}, \sin\theta_{ei} - \sin\theta_{ei}^d \le e_{Rz},\end{aligned} \tag{D.2}$$

where e_{Rx}, e_{Ry}, and e_{Rz} are positive constants. Substituting Eq. (D.2) into Eq. (D.1) then yields

$$\begin{aligned}\dot{V}_{pi} \le &\, e_{xi}\left(U_i\cos\psi_{ei}^d\cos\theta_{ei}^d - U_0 + f_{xi} + U_i e_{Rx}\right) \\ &+ e_{zi}\left(-U_i\sin\theta_{ei}^d + f_{zi} + U_i e_{Rz}\right) \\ &+ e_{yi}\left(U_i\sin\psi_{ei}^d + f_{yi} + U_i\left(e_{Ry} + \theta_{ei}^d h\left(\psi_{ei}^d, \theta_{ei}^d\right)\right)\right)\end{aligned} \tag{D.3}$$

where $h\left(\psi_{ei}^d, \theta_{ei}^d\right) = \sin\psi_{ei}^d\left(\cos\theta_{ei}^d - 1\right)/\theta_{ei}^d$ is an auxiliary function. Given that $\left|\left(\cos\theta_{ei}^d - 1\right)/\theta_{ei}^d\right| < 0.73$, it is guaranteed that $\left|h\left(\psi_{ei}^d, \theta_{ei}^d\right)\right| < 1$. Introducing Eq. (10) into Eq. (D.3) then yields

$$\begin{aligned}\dot{V}_{pi} \le &\, e_{xi}\left(\frac{U_i}{\Delta_i} - U_0 + f_{xi} + U_i e_{Rx}\right) + e_{zi}\left(-U_i\frac{\hat{e}_{zi} + \delta_{zi}}{\Delta_i\Delta_y} + f_{zi} + U_i e_{Rz}\right) \\ &+ e_{yi}\left(-U_i\frac{\hat{e}_{yi} + \delta_{yi}}{\Delta_z} + f_{yi} + U_i\left(e_{Ry} + \left|\theta_{ei}^d\right|\right)\right).\end{aligned} \tag{D.4}$$

Based on Eq. (11), it follows that $\hat{U}_i\delta_{yi}/\Delta_z = \hat{f}_{yi}$ and $\hat{U}_i\delta_{zi}/\Delta_i\Delta_y = \hat{f}_{zi}$. Under Theorems 1 and 2, it can be deduced that $\tilde{U}_i = \hat{U}_i - U_i$, $\tilde{f}_{xi} = \hat{f}_{xi} - f_{xi}$, $\tilde{f}_{yi} = \hat{f}_{yi} - f_{yi}$, and $\tilde{f}_{zi} = \hat{f}_{zi} - f_{zi}$ are ultimately bounded. It can be further proven that $\left|\tilde{f}_{xi}\right| \le e_{fx}$, $\left|-U_i\delta_{yi}/\Delta_z + f_{yi}\right| \le e_{fy}$, $\left|-U_i\delta_{zi}/\Delta_i\Delta_y + f_{zi}\right| \le e_{fz}$, where e_{fx}, e_{fy}, and e_{fz} are positive constants. Moreover, one has $U_i = \frac{u_i}{\cos\alpha_i\cos\beta_i} = \frac{u_i^d + e_{ui}}{\cos\alpha_i\cos\beta_i}$. Thus, Eq. (D.4) can be rewritten as

$$\begin{aligned}\dot{V}_{pi} \le &\, e_{xi}\left(-b_u e_{xi} - b_u\tilde{e}_{xi} + \tilde{U}_{i0} + e_{fx} + U_i e_{Rx} + f_{ui}\right) \\ &+ e_{zi}\left(-U_i\frac{e_{zi}}{\Delta_i\Delta_y} + e_{fz} + U_i\left(e_{Rz} - \frac{\tilde{e}_{zi}}{\Delta_i\Delta_y}\right)\right) \\ &+ e_{yi}\left(-U_i\frac{e_{yi}}{\Delta_z} + e_{fy} + U_i\left(e_{Ry} + \left|\theta_{ei}^d\right| - \frac{\tilde{e}_{yi}}{\Delta_z}\right)\right) \\ \le &-\boldsymbol{e}_{pi}^T\boldsymbol{L}_{pi}\boldsymbol{e}_{pi} + \boldsymbol{e}_{pi}^T\boldsymbol{M}_{pi}\end{aligned} \tag{D.5}$$

where $\boldsymbol{L}_{pi} = \begin{pmatrix} b_u & 0 & 0 \\ 0 & \frac{U_i}{\Delta_z} & 0 \\ 0 & 0 & \frac{U_i}{\Delta_i\Delta_y} \end{pmatrix}$ and $\boldsymbol{M}_{pi} = [\, -b_u\tilde{e}_{xi} + \tilde{U}_{i0} + e_{fx} + U_i e_{Rx} + f_{ui}, e_{fy} + U_i\left(e_{Ry} + \left|\theta_{ei}^d\right| - \frac{\tilde{e}_{yi}}{\Delta_z}\right), e_{fz} + U_i\left(e_{Rz} - \frac{\tilde{e}_{zi}}{\Delta_i\Delta_y}\right)]^T$, $\tilde{e}_{xi} = \hat{e}_{xi} - e_{xi}$, $\tilde{e}_{yi} = \hat{e}_{yi} - e_{yi}$, $\tilde{e}_{zi} = \hat{e}_{zi} - e_{zi}$, $\tilde{U}_{i0} = \hat{U}_{i0} - U_{i0}$ and $f_{ui} = e_{ui}/(\cos\alpha_i\cos\beta_i\Delta_i)$. Note that $\tilde{e}_{xi}$, $\tilde{e}_{yi}$, $\tilde{e}_{zi}$, $\tilde{U}_{i0}$ are estimation errors induced by the DO, which are guaranteed to be bounded and converge to zero in finite time, e_{fx}, e_{fy}, e_{fz} are estimation errors induced by the CESO, and $e_{Rx}, e_{Ry}, e_{Rz}, f_{ui}$ are tracking errors induced by the dynamic controller. According to Theorems 1–3, these error signals all converge to a small neighborhood around zero. In other words, $\left\|\boldsymbol{M}_{pi}\right\|$ is lower and upper bounded by a positive constant and M_{pi}, respectively, and the upper bound $\bar{M}_{pi}$ can be minimized by adjusting controller parameters according to the guidelines given in Appendix E. Consequently, it can be concluded that $\left\|\boldsymbol{e}_{pi}\right\| \le \bar{M}_{pi}/\lambda_{\min}\left(\boldsymbol{L}_{pi}\right)$. ■

Appendix E. A discussion of control parameters

In this section, some guidelines for the observer and control parameters are provided to help readers compromise between tracking accuracy, transient response, saturation avoidance, and estimation performance.

E.1. Observer parameters

For DO Eq. (6), $\boldsymbol{K}_\eta$ should be a diagonal positive definite matrix. The increase of $\boldsymbol{K}_\eta$ can speed up the estimation process, as shown in Eq. (A.1), but large values might result in instability. In addition, it is required that $\kappa_1 > \gamma_\Phi$, $\kappa_2 > 0$ and ς satisfies $0 < \varsigma = \varsigma_1/\varsigma_2 < 1$ with ς_1 and ς_2 being positive odd integers. The increase of κ_1 will amplify noncontinuous signal $sign\left(\boldsymbol{\mu}_{\eta i}\right)$, which might lead to chattering phenomena. From Appendix A, larger value of κ_2 can reduce the settle time. In summary, $\boldsymbol{K}_\eta$ should be increased gradually to achieve the desired estimation response, and κ_1 can be tuned according to γ_Φ.

For CESO Eqs. (7), (8), and (9), the gains can be chosen as $k_{q1} = 3\omega_q$, $k_{q2} = 3\omega_q^2$, $k_{q3} = \omega_q^3$, $k_{r1} = 3\omega_r$, $k_{r2} = 3\omega_r^2$, $k_{r3} = \omega_3^3$, and

$\boldsymbol{K}_{p1} = 3\omega_p \boldsymbol{I}_3, \boldsymbol{K}_{p2} = 3\omega_p^2 \boldsymbol{I}_3, \boldsymbol{K}_{p3} = \omega_p^3 \boldsymbol{I}_3$, where ω_q, ω_r, and ω_p are observer bandwidths. By referring to the proof of Theorem 2, it can be noticed that the estimation error can be tuned to be arbitrarily small by increasing the observer bandwidths. However, the bandwidths are normally limited due to measurement noise. This is an unavoidable shortcoming of ESOs. Therefore, ω_q, ω_r, and ω_p should be tuned by taking into consideration both sensitivity to noise and the estimation performance.

E.2. Control parameters

Regarding the LOS guidance law Eq. (10), and according to Eq. (D.5), the decrease of Δ_y can reduce the response time and minimize the tracking error. However, small Δ_y values will also lead to large velocity command signals, which may violate the system constraints. Consequently, Δ_y should be determined by compromising between tracking accuracy and saturation.

For kinematic controller Eq. (12), larger values of gains b_u, b_θ, and b_ψ guarantee better tracking accuracy, but system constraints might also be violated as gains increase. A trade off between tracking accuracy and saturation should therefore also be considered when tuning these gains.

For dynamic controller Eq. (13), $c_q > 0$, $2w_1 > w_2$, and $2l_1 > c_q + l_2$ should first be satisfied. The increase of c_q can improve the velocity tracking accuracy, but might also increase the control input amplitude, leading to input saturation. An increase of w_2 and l_2 can enhance controller sensibility against saturation, and an increase of w_1 and w_2 can improve robustness against saturation. However, for the sake of stability, the gains cannot be too large.

References

[1] Scheidler A, Brutschy A, Ferrante E, Dorigo M. The k-unanimity rule for self-organized decision-making in swarms of robots. IEEE Trans Cybern 2015;46(5):1175–88.

[2] Zhang Y, Wang X, Wang S, Tian X. Three-dimensional formation–containment control of underactuated auvs with heterogeneous uncertain dynamics and system constraints. Ocean Eng 2021;238:109661.

[3] Valentini G, Ferrante E, Dorigo M. The best-of-n problem in robot swarms: Formalization, state of the art, and novel perspectives. Front Robot AI 2017;4(9):1–18.

[4] Ferrante E, Turgut AE, Huepe C, Stranieri A, Pinciroli C, Dorigo M. Self-organized flocking with a mobile robot swarm: a novel motion control method. Adapt Behav 2012;20(6):460–77.

[5] Zhang Y, Wang X, Wang S, Tian X. Distributed bearing-based formation control of unmanned aerial vehicle swarm via global orientation estimation. Chin J Aeronaut 2022;35(1):44–58.

[6] Dorigo M, Theraulaz G, Trianni V. Reflections on the future of swarm robotics. Sci Robot 2020;5(49):eabe4385.

[7] Zhu W, Allwright M, Heinrich MK, Oğuz S, Christensen AL, Dorigo M. Formation control of UAVs and mobile robots using self-organized communication topologies. In: International conference on swarm intelligence. Springer; 2020, p. 306–14.

[8] Jamshidpey A, Zhu W, Wahby M, Allwright M, Heinrich MK, Dorigo M. Multi-robot coverage using self-organized networks for central coordination. In: International conference on swarm intelligence. Springer; 2020, p. 216–28.

[9] Yang Y, Xiao Y, Li T. A survey of autonomous underwater vehicle formation: performance, formation control, and communication capability. IEEE Commun Surv Tutor 2021;23(2):815–41.

[10] Liang Q, Ou J, Xue Z, Ippolito C. Influences of temperature and salinity on holistic network performability of multi-AUV cooperative systems. ISA Trans 2019;93:165–71.

[11] Paull L, Saeedi S, Seto M, Li H. AUV navigation and localization: A review. IEEE J Ocean Eng 2013;39(1):131–49.

[12] Wu Y, Ta X, Xiao R, Wei Y, An D, Li D. Survey of underwater robot positioning navigation. Appl Ocean Res 2019;90:101845.

[13] Meurer C, Fuentes-Pérez JF, Palomeras N, Carreras M, Kruusmaa M. Differential pressure sensor speedometer for autonomous underwater vehicle velocity estimation. IEEE J Ocean Eng 2019;45(3):946–78.

[14] Peng Z, Wang J, Wang J. Constrained control of autonomous underwater vehicles based on command optimization and disturbance estimation. IEEE Trans Ind Electron 2018;66(5):3627–35.

[15] Zheng Z, Sun L, Xie L. Error-constrained LOS path following of a surface vessel with actuator saturation and faults. IEEE Trans Syst Man Cybern-Syst 2017;48(10):1794–805.

[16] Peng Z, Wang J, Han Q-L. Path-following control of autonomous underwater vehicles subject to velocity and input constraints via neurodynamic optimization. IEEE Trans Ind Electron 2018;66(11):8724–32.

[17] Li H, Xie P, Yan W. Receding horizon formation tracking control of constrained underactuated autonomous underwater vehicles. IEEE Trans Ind Electron 2016;64(6):5004–13.

[18] Wang J, Wang C, Wei Y, Zhang C. Sliding mode based neural adaptive formation control of underactuated AUVs with leader-follower strategy. Appl Ocean Res 2020;94:101971.

[19] Yuan C, Licht S, He H. Formation learning control of multiple autonomous underwater vehicles with heterogeneous nonlinear uncertain dynamics. IEEE Trans Cybern 2018;48(10):2920–34.

[20] Xia G, Zhang Y, Zhang W, Chen X, Yang H. Dual closed-loop robust adaptive fast integral terminal sliding mode formation finite-time control for multi-underactuated AUV system in three dimensional space. Ocean Eng 2021;233:108903.

[21] Li J, Du J, Lewis FL. Distributed three-dimension time-varying formation control with prescribed performance for multiple underactuated autonomous underwater vehicles. Internat J Robust Nonlinear Control 2021;31(13):6272–87.

[22] Wang J, Wang C, Wei Y, Zhang C. Bounded neural adaptive formation control of multiple underactuated AUVs under uncertain dynamics. ISA Trans 2020;105:111–9.

[23] Wei H, Shen C, Shi Y. Distributed Lyapunov-based model predictive formation tracking control for autonomous underwater vehicles subject to disturbances. IEEE Trans Syst Man Cybern-Syst 2019;51(8):5198–208.

[24] Shojaei K. Neural network formation control of underactuated autonomous underwater vehicles with saturating actuators. Neurocomputing 2016;194:372–84.

[25] Wang J, Wang C, Wei Y, Zhang C. Observer-based neural formation control of leader–follower AUVs with input saturation. IEEE Syst J 2020;15(2):2553–61.

[26] Liang H, Fu Y, Gao J, Cao H. Finite-time velocity-observed based adaptive output-feedback trajectory tracking formation control for underactuated unmanned underwater vehicles with prescribed transient performance. Ocean Eng 2021;233:109071.

[27] Kim JH, Yoo SJ. Distributed event-triggered adaptive output-feedback formation tracking of uncertain underactuated underwater vehicles in three-dimensional space. Appl Math Comput 2022;424:127046.

[28] Hu Z, Ma C, Zhang L, Halme A, Hayat T, Ahmad B. Formation control of impulsive networked autonomous underwater vehicles under fixed and switching topologies. Neurocomputing 2015;147:291–8.

[29] Yan Z, Yang Z, Yue L, Wang L, Jia H, Zhou J. Discrete-time coordinated control of leader-following multiple AUVs under switching topologies and communication delays. Ocean Eng 2019;172:361–72.

[30] Yan Z, Zhang C, Tian W, Zhang M. Formation trajectory tracking control of discrete-time multi-AUV in a weak communication environment. Ocean Eng 2022;245:110495.

[31] Peng Z, Wang J. Output-feedback path-following control of autonomous underwater vehicles based on an extended state observer and projection neural networks. IEEE Trans Syst Man Cybern-Syst 2017;48(4):535–44.

[32] Ni W, Cheng D. Leader-following consensus of multi-agent systems under fixed and switching topologies. Syst Control Lett 2010;59(3–4):209–17.

[33] Do KD, Pan J. Control of ships and underwater vehicles: design for underactuated and nonlinear marine systems. Vol. 1, Springer; 2009.

[34] Dong X, Hu G. Time-varying formation control for general linear multi-agent systems with switching directed topologies. Automatica 2016;73:47–55.

[35] Dong X, Zhou Y, Ren Z, Zhong Y. Time-varying formation tracking for second-order multi-agent systems subjected to switching topologies with application to quadrotor formation flying. IEEE Trans Ind Electron 2016;64(6):5014–24.

[36] Miao J, Wang S, Zhao Z, Li Y, Tomovic MM. Spatial curvilinear path following control of underactuated AUV with multiple uncertainties. ISA Trans 2017;67:107–30.

[37] Zhang Y, Wang X, Wang S, Miao J. DO-LPV-based robust 3D path following control of underactuated autonomous underwater vehicle with multiple uncertainties. ISA Trans 2020;101:189–203.

[38] Miao Z, Liu Y-H, Wang Y, Yi G, Fierro R. Distributed estimation and control for leader-following formations of nonholonomic mobile robots. IEEE Trans Autom Sci Eng 2018;15(4):1946–54.

[39] Hua Y, Dong X, Wang J, Li Q, Ren Z. Time-varying output formation tracking of heterogeneous linear multi-agent systems with multiple leaders and switching topologies. J Frankl Inst-Eng Appl Math 2019;356(1):539–60.
[40] Cai H, Huang J. The leader-following consensus for multiple uncertain Euler-Lagrange systems with an adaptive distributed observer. IEEE Trans Automat Control 2015;61(10):3152–7.
[41] He C, Huang J. Adaptive distributed observer for general linear leader systems over periodic switching digraphs. Automatica 2022;137:110021.
[42] Liu L, Wang D, Peng Z. ESO-based line-of-sight guidance law for path following of underactuated marine surface vehicles with exact sideslip compensation. IEEE J Ocean Eng 2016;42(2):477–87.
[43] Yu S, Yu X, Shirinzadeh B, Man Z. Continuous finite-time control for robotic manipulators with terminal sliding mode. Automatica 2005;41(11):1957–64.
[44] Wang X, Hong Y. Distributed finite-time χ-consensus algorithms for multi-agent systems with variable coupling topology. J Syst Sci Complex 2010;23(2):209–18.